Chapter 2: Identification of matrix metalloproteinase-9 inhibitors

2.1 Introduction

Matrix metalloproteinases (MMPs) are a group of 25 closely related human homologous calcium-mediated and zinc-dependent membrane-bound extracellular endopeptidases. They are involved in extracellular matrix (ECM) degradation, tissue remodeling, organogenesis, growth, and normal tissue turn over. The imbalance inactivity of MMPs may result in several pathophysiological conditions. Human MMP-9, also familiar as gelatinase B, contributes to the progression of extracranial arteriovenous malformations (AVMs) [1], rheumatoid arthritis [2], several neurological diseases, inflammatory processes [3], cancer [4, 5] and ischemic stroke [6-8]. It is also associated with the pathophysiological processes that develop during ischemic stroke: blood-brain barrier (BBB) destruction [9], edema formation [10], activation of proinflammatory cytokines (tumor necrosis factor-α, interleukin-1β) [10], and elimination of myelin proteins [11]. S1′ pocket, the selectivity site of MMPs, is a highly preserved catalytic domain and differs mostly in the amino acid sequence [12]. It is represented in the substrate preferences of depthless MMPs pocket (MMP-1, 7) compared to deep MMPs pocket (MMP-2, 3, 8, 9, 12, and 13). The significant difference in the selectivity S1′ pocket in MMP-2 is residues 427–433. MMP-9 forms structurally different loop (residues 425–431) [13] that are equivalent in MMP-2 structure. The MMP inhibitors have failed in clinical trials [14] because of the lack of inhibitor specificity of homogeneous MMPs. Further, the critical adverse effect of the treatment may be due to the presence of hydroxamate as a zinc-binding group (ZBG) that can chelate the zinc and also other divalent cations.

The potent MMP-13 inhibitors, ZINC 02535232, ZINC 08399795, ZINC 12419118 and ZINC 00624580 were discovered, that produced H-bond interactions in the crystal structure of 1XUC with reasonable RMSD values exhibiting a unique interaction pattern not observed previously [15]. Pradiba D. *et al.* studied the binding modes of flavonols with the active site of MMP-9 through molecular docking, post-docking MM-GBSA, and molecular dynamic (MD) simulations. They reported gossypin as a hopeful candidate for MMP-9 inhibition with a docking score of −14.618 kcal mol^{-1}, and binding energy of −79.97 kcal mol^{-1} [16]. Scorpion toxins, *i.e.*, chlorotoxin (ClTx) and AaCTx, interacted with MMP-2 to inhibit glioma cell invasion by molecular modeling, molecular dynamics, and MM-PB(GB)SA free energy estimation [17]. Wang *et al.* identified four-potential dual MMP-2/HDAC-6 inhibitors, *i.e.*, STOCK1N-46177, STOCK1N-52245, STOCK1N-55477, and STOCK1N-69706 from natural sources by hierarchical virtual screening [18]. Molecular dynamics (MD) study of the properties of MMP-1-collagen crystallographic structure, followed by an exploration of the free energy surface of a collagen polypeptide chain entering the active site, using a combined meta-dynamics and umbrella sampling (MDUS) approach were also performed [19]. Hinokiflavone had been screened from the natural compound database utilizing a ligand-based pharmacophore model [20]. It had stable interaction with high binding free energy of −26.54 $kJ.mol^{-1}$ at S1 loop of MMP-9 and acted as an anticancer agent.

The *in-silico* approaches help to identify better hits and scaffolds for a selective target with less toxicity. In this study, highly specific, less toxic, non-ZBG inhibitors of MMP-9 were searched from e-pharmacophore, and ligand-based (3D-QSAR) approaches. The flowchart of hits identification by structure- and ligand-based drug design is given in **Figure 2.1**

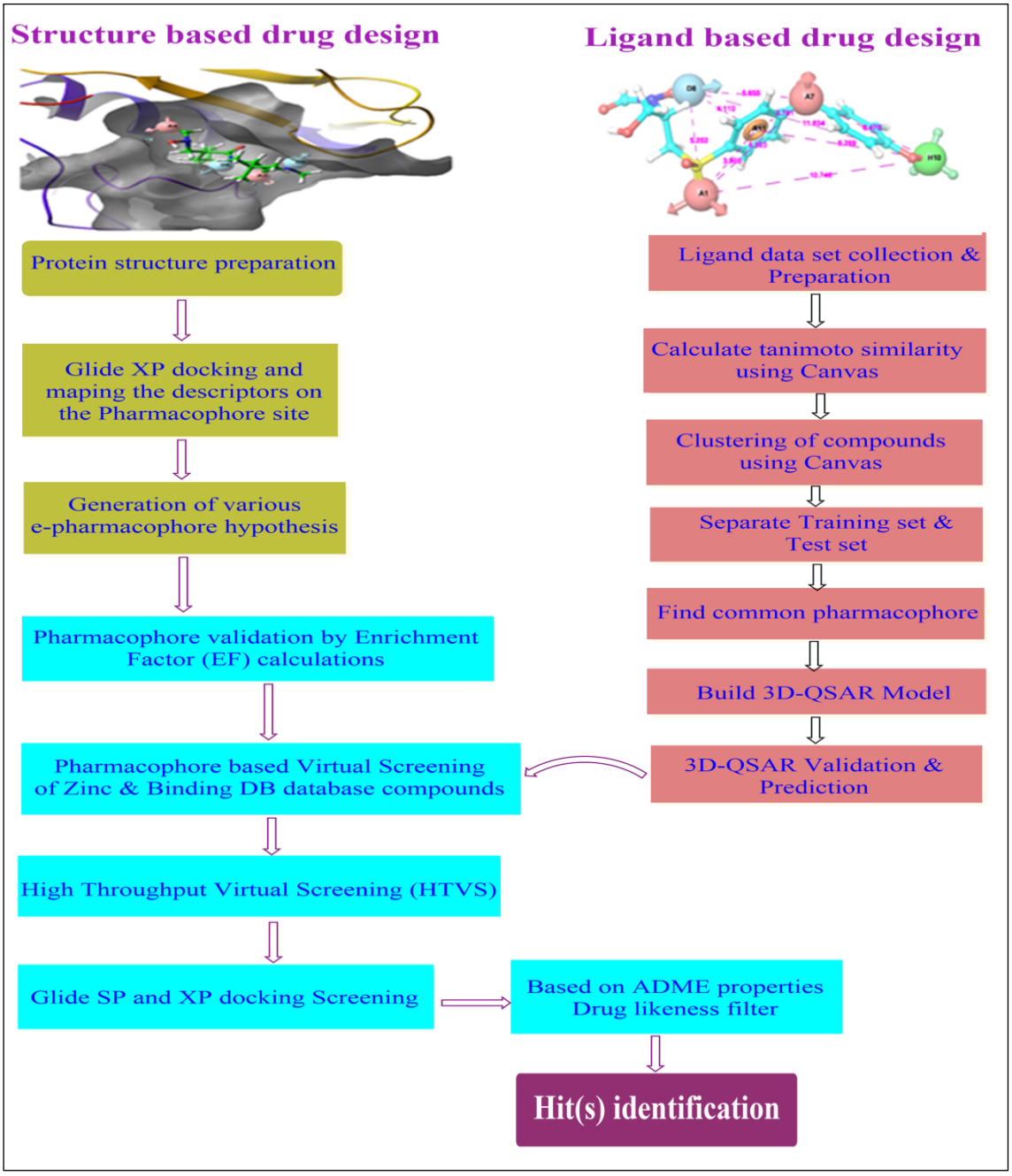

Figure 2.1 Hit(s) identification workflow by structure-based and ligand-based drug design.

2.2 Materials and Methods

2.2.1 Computational details

The computational tasks, except MD, were performed on an Intel(R) Core (TM) i5-3210M CPU @ 2.50 GHz processor with a memory of 8.0 GB RAM running on a Linux 64 operating system. Schrödinger suite 2015-1 (Schrödinger, LLC, New York,

NY, 2015) was utilized to develop structure-based and ligand-based pharmacophore models and also for the screening of the free 'ZINC15' database. MD simulation was performed by using Desmond package on an Intel(R) Xeon(R) CPU E3-1225v5@ 3.30 GHz 3.31 GHz processor, RAM 32.0 GB system with Nvidia 'Quadro P600' GPU running on a Linux 64 operating system.

2.2.2 Energetically optimized structure-based pharmacophore generation

The energetically optimized structure-based pharmacophore attains advantage of both ligand- and structure-based methods that can be used to screen millions of compounds rapidly. The e-Pharmacophore allows for excluded volumes that correspond to regions which are occupied by the enzyme structure. It is a robust tool for hit hopping to retrieve more diverse set of actives, than traditional structure-based pharmacophore methods. The e-pharmacophore generation involves two steps: the first step constitutes the generation of pharmacophoric sites and second step includes ranking by their energetic contribution for binding, after calculating the Glide XP energy terms to the pharmacophoric aspects of the ligand [21].

2.2.2.1 Protein structure preparation

Ten X-ray structures of human MMP-9 out of total 21, (**Table 2.1**) bound with various ligands were collected from the Protein Data Bank (PDB) [22] (http://www.rcsb.org). Further, five PDB structures *viz.* (i) **4XCT** [ligand (S)-N-isopropoxy-N-(3-methl-1-nitroso-1-oxobutan-2-yl)-[1,1′-biphenyl]-4-sulonamide]; (ii) **4WZV** [ligand (2R)-4-(1,3-dioxo-1,3-dihydro-2H-isoindol-2-yl)-N-hydroxy-2-[[(4'-methoxybiphenyl-4-yl) sulfonyl](propan-2-yloxy)amino]butanamide]; (iii) **2OVX** [ligand 5-(4-phenoxyphenyl) 5-(4-pyrimidin-2-ylpiperazin-1-yl)pyrimidine-2,4,6(2h,3h)-trione]; (iv) **2OW1** [ligand (2R)-2-amino-3,3,3-trifluoro-N-hydroxy-2-[[(4-phenoxyphenyl)sulfonyl]methyl]propen amide]; and (v) **1GKC** [ligand N-2-[(2R)-2-[[formyl(hydroxy) amino] methyl]-4-

methylpentanoyl]-N,3-dimethyl-L-valinamide] were selected on the basis of structural resolution and MMP-9 enzyme inhibition activity (IC_{50} value/K_i value) of cocrystal ligand.

Table 2.1 Crystal structures of human matrix metaloproteinase-9 with cocrystal ligands

PDB	Resolution (Å)	Cocrystal ligand[a]	SMILES structure of cocrystal ligand	IC_{50} (nM) MMP-9	IC_{50} (nM) MMP-2
4XCT	1.3	N73[23]	[H]OS(N(OC(C)C)[C@@H](C(C)C)C(N=O)=O)(O[H])C(C=C1)=CC=C1C2=CC=CC=C2	6.7	0.81
4WZV	1.65	E40 [23]	O=S(C1=CC=C(C2=CC=C(OC)C=C2)C=C1)(N([C@H](C(N(O[H])[H])=O)CCN(C(C3=C4C=CC=C3)=O)C4=O)OC(C)C)=O	0.43	0.67
4H3X	1.76	10B [24]	O=S(N(CC(N([H])O[H])=O)OC(C)C)(C1=CC=C(C2=CC=CC=C2)C=C1)=O	200	12
5CUH	1.83	LTQ [25]	O=C([C@H]1CSCN1S(=O)(N2CCN(C3=C(C)C=C(C#N)C=C3)CC2)=O)N([H])O[H]	24000	5400
2OVX	2.00	4MR [26]	O=C(N([H])C(N([H])C1=O)=O)C1(N2CCN(C3=NC=CC=N3)CC2)C4=CC=C(C=C4)OC5=CC=CC=C5	2	5
2OW0	2.00	6MR [26]	O=C(O[H])[C@H](N([H])S(=O)(C1=CC=C(C2=CC=C(I)C=C2)C=C1)=O)CC3=CN([H])C4=CC=CC=C43	201	9.3
2OW1	2.20	7MR [26]	O=S(C1=CC=C(C=C1)OC2=CC=CC=C2)(C[C@](N([H])[H])(C(N([H])O[H])=O)C(F)(F)F)=O	1.0	0.01
2OW2	2.90	8MR [26]	COC1=CC=C(S(=O)([C@@H](C(F)F)CC(O[H])=O)=O)C=C1	6	730
2OVZ	2.00	5MR [26]	O=C(N([H])[H])[C@H](N([H])C([C@H](CC1=CC(C2=CC=CC=C2)=NO1)C[P@](O[H])(C3=CC=CC=C3)=O)=O)CC4=CN([H])C5=CC=CC=C54	13 [b]	12 [b]
1GKC	2.30	NFH[27]	O=C(N([C@H](C(C)(C)C)C(N(C)[H])=O)[H])[C@@H](CC(C)C)CN(C([H])=O)O[H]	21 [b]	–

[a]Cocrystal ligand code reported in RCSB wave site; [b]Ki value instead of IC_{50}.

Protein preparation wizard in Maestro 10.1 (Schrödinger, LLC, New York, NY, 2015) was utilized to prepare the crystal protein structures, using default setting with

OPLS_2005 as a force field [28]. The cocrystal ligands with PDB ID, resolution and inhibitory activity (IC_{50} value/Ki value) are included in **Figure 2.2**.

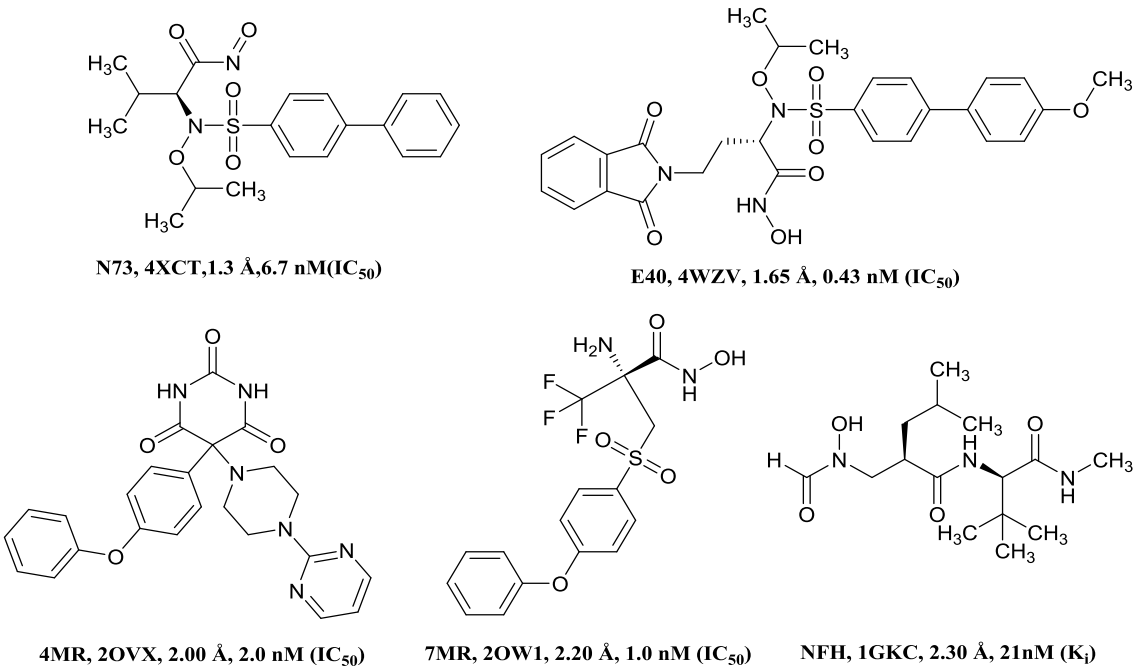

Figure 2.2 Cocrystal inhibitor structures from MMP-9 structure for the development of e-pharmacophore with their respective PDB, resolutions, and inhibitory activity (IC_{50} value /Ki value).

2.2.2.2 Development of e-pharmacophore hypothesis

The Grids of all five prepared crystal structures were generated utilizing Receptor Grid Generation tools in Maestro at centroid of cocrystal ligands. The crystal ligands were refined and Glide XP (extra precision) docking was performed with respective protein structure using Glide (Schrödinger, LLC, New York, NY, 2015). Metal and metal coordination constraints were used with other default settings during Grid generation and Glide XP docking, as a zinc atom interacting with ligand and receptor in MMPs. PHASE v4.2 (Schrödinger, LLC, New York, NY, 2015) was employed to develop pharmacophore features utilizing the XP descriptor information. Hydrogen-bond acceptor (A), hydrogen-bond donor (D), hydrophobic group (H), negative ionizable group (N), positive ionizable group (P), and aromatic ring (R) in PHASE were utilized

to generate pharmacophore sites. Hydrogen-bond acceptor and hydrogen-bond donor sites were pictured as vectors directed to the corresponding hydrogen-bond donor and acceptor positions at the binding site of enzymes respectively. Glide XP descriptors consist of a hydrophobic enclosure, hydrophobically packed associated hydrogen bonds, electrostatic rewards, π−π stacking, π−cation, and other interactions. The most favorable sites were preferred by these energies for the pharmacophore hypothesis and were used for virtual screening [21]. Initially, ten pharmacophore sites were designed for all the crystal structures. When an energetic value of pharmacophore feature site was equal to the sum of the Glide XP energies from the site of atoms comprising, then pharmacophore feature site was quantified and ranked based on its energetic value. The pharmacophore sites with less than half of the heavy atoms contributing to the pharmacophore feature were excluded from the final hypothesis. The variations in this rule, *i.e.*, including the features with fewer than half of the heavy atoms exhibiting energetic interactions, were tried and tested during this work but that did not show any improvement in enrichment. The procedure reported here is thus based on the final energy optimized hypotheses (e-pharmacophores) [21].

2.2.3 Enrichment calculations

Enrichment factor (EF) is known as the fraction of known actives, that recover when a fraction of the database is screened [29]. EF(X%) is the fraction of known actives return after X% of database has been screened and was initially concentrated on EF(1%) [21]. The developed e-pharmacophores were validated to determine accuracy by calculating enrichment factor (EF) and goodness of hit (GH) (Equation **2.1** and **2.2** respectively) using a prepared compounds' dataset. The dataset was prepared using 1000 drug-like decoys (http://www.schrodinger.com/glide_decoy_set) with an average molecular weight of 400 D (the "dl-400" data set) and 90 known actives of MMP-9 inhibitors with

IC_{50} less than 100 nM. The actives were not utilized for the QSAR model. The dataset compounds were prepared by using Ligprep (Maestro 10.1, Schrödinger, LLC, New York, NY, 2015). The Boltzmann-enhanced discrimination of receiver operating characteristic (BEDROC), another enrichment metrics, was also utilized to ensure that the results from e-pharmacophore were significant [30]. The values of α, 8.0, 20.0 and 160.9 were used for comparison, and 20.0 value was found as a reasonable choice for virtual screening.

$$EF = \frac{Ha \times D}{Ht \times A} \quad \ldots\ldots\ldots\ldots\ldots\ldots\ldots\ldots\ldots\ldots\ldots\ldots (2.1)$$

$$\mathrm{GH} = \left[\frac{(\mathrm{Ha}(3\mathrm{At} + \mathrm{Ht})}{4\mathrm{HtA}}\right]\left[1 - \frac{(\mathrm{Ht} - \mathrm{Ha})}{(\mathrm{D} - \mathrm{A})}\right] \ldots\ldots\ldots (2.2)$$

Where 'EF' is enrichment factor, 'GH' is the goodness of hit, 'D' is total compounds in the data set, 'A' is a total number of actives in the data set, 'Ht' is total hits, and 'Ha' is number of active hits.

2.2.4 Ligand-based pharmacophore generation

1.1.1.1 Preparation of data sets for development of the hypothesis

The known and wide range of IC_{50} values (0.01−352000 nM) of total 1650 MMP-9 inhibitors with structural diversity were collected from BindingDB (http://www.bindingdb.org) and literature [31-66]. The default setting of LigPrep in Maestro was applied to minimize the energy of inhibitors utilizing force field OPLS_2005. Based on Tanimoto similarities, all the compounds were clustered by Hierarchical method with structurally diverse molecules using linear fingerprint descriptors in Canvas v2.3 (Schrödinger, LLC, New York, NY). Further, 155 compounds (Appendix; **Figure A.1**), depending upon the canvas similarity against N-Isobutyl-N-(4-methoxyphenylsulfonyl)glycyl hydroxamic acid (NNGH), were preferred

from 33 clusters of representative compounds. The IC_{50} values of compounds were converted to pIC_{50} for the generation of 3D-QSAR model.

2.2.4.1 Generation of 3D-QSAR model

PHASE v4.2 was employed to develop the 3D-QSAR model and statistical analyses. The ConfGen (Schrödinger, LLC, New York, NY, 2015) was used to generate conformers. Maximum 1000 conformers per structure were generated utilizing force field OPLS_2005 with constant distance-dependent dielectric solvent, relative energy of 10.0 kcal mol^{-1} and an RMSD of 1Å. The pharmacophore sites were created on each compound based on the presence of interacting group on ligand. The threshold of the active was above 8.6 and inactive was below 7.0. The common pharmacophores thus obtained, were ranked by the score of hypotheses to identify the pharmacophore from each surviving n-dimensional box having the best alignment of the active set ligands. The more significant difference in scores between active and inactive developed better hypothesis in differentiating the active from inactive [67]. All 155 inhibitors were aligned with the template pharmacophore hypothesis with a high active score (**Figure 2.3**).

Total 155 molecules (Appendix; **Table A.1**) were divided randomly into two sets, *i.e.*, the test set containing 31 molecules and the training set of 124, by applying Automated Random Selection method in the Phase to develop 3D-QSAR model. The partial least-squares (PLS) regression was applied to a set of binary variables of different pharmacophore features in the training set [68]. The Atom-based 3D-QSAR models were developed using the diverse structures of 124 training set of ligands with 1.00 Å of grid spacing. The predicted activities of 31 test set compounds were used to validate QSAR models. The models with PLS factors one to five were developed, and PLS factor 5 was observed as the best model, that was statically validated* [69].

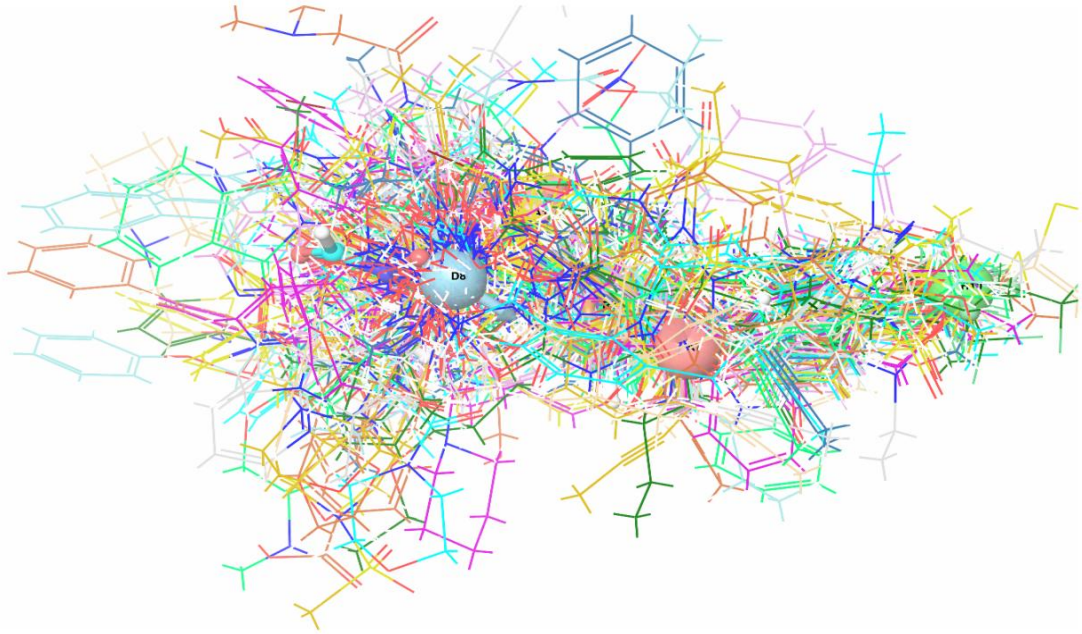

Figure 2.3 Alignment of all 155 ligands on the pharmacophore model AADHR of 3D-QSAR.

2.2.5 External validation of 3D-QSAR models

The "leave one out" (LOO) method was adopted for the cross-validation analysis of the 3D-QSAR models to evaluate the predictive ability [21, 70]. The top three QSAR models and the respective pharmacophores were employed to find new hit molecules, due to their excellent predictivity*.

*The R^2 (square of correction coefficient) and Q^2 (Q square of predicted activity) values are higher than 0.8 and 0.6 respectively and are acceptable.

2.2.6 Database preparation

Ligand-based pharmacophore and e-pharmacophore based screening of compounds were performed against 35,30,908 compounds collected from 'Zinc 15' Database without known MMP-9 inhibitors (http://zinc.docking.org). The database compounds were prepared using LigPrep in Maestro utilizing force field OPLS_2005 and generated possible state employing Epik (Schrödinger, LLC, New York, NY, 2015) with 'Add metal-binding states.'

2.2.7 Pharmacophore-based screening of the database

Ligand-based pharmacophore and e-pharmacophore matching were required for the most energetically favorable site, scoring better than −1.0 kcal mol^{-1}. For the screening of database molecules, all the sites of hypotheses were required to match. The distance matching tolerance was set up to 2.0 Å. The pharmacophore matched database was ranked in order of the fitness score ranging from zero to three, as employed in PHASE default database screening. The aligned compound conformer matches the hypothesis based on fitness score which expressed rmsd, site matching, vector alignments, and volume terms [67]. The ligands were selected based on the fitness scores and scores above 1.0 were considered as good inhibitors. The molecules with the best fitness score were docked into the binding sites of MMP-9 protein structure [21].

2.2.8 Removal of pan-assay interference compounds

Baell and Holloway reported a list of structural features, which generated frequent false positives across screening, known as PAINS [71]. Jasial S. *et al.* established a large-scale analysis of behavior of PAINS in biological screening assays [72]. The PAINS free 'ZINC15' database molecules categorized within (A) anodyne, and (B) clean (PAINS-ok) [73], were selected as hits from HTVS retrieves. A KNIME (freely available Konstanz Information Miner, http://knime.org) [74] workflow distributed with RDKit [75] software package utilizing GUI data analysis platform was developed by Saubern S. *et al.* [76]. The obtained HTVS hits were screened *in silico* for PAINS to avoid false positives in biochemical and pharmacological assays using three public filters, *i.e*., RDKit [75], ZINC [73] and FAF-Drugs4 server [77].

2.2.9 High-throughput virtual screening and molecular docking

The pharmacophore matched database was docked into the binding sites of respective crystal structures of MMP-9 using Glide in Maestro with high-throughput virtual

screening (HTVS). Glide HTVS is faster, has higher tolerance to unacceptable fits than Glide SP (standard precision) as well as XP (extra precision) and thus is suited for the study [29]. The Grid of previously prepared crystal structures were developed at the center of the cocrystal ligand using metal and metal coordination constraints with other default settings. The Glide HTVS was performed using metal constraints with prepared database compounds. The molecules with the best docking and Glide scores of HTVS were selected for Glide SP and XP screenings. After HTVS, all the non-peptide retrieves were isolated, and XP docking was performed using 4XCT crystal structure to compare the docking score of retrieves. The 4XCT crystal structure of MMP-9 was selected for comparative study of hits, because of its lowest resolution (1.3Å) and cocrystal ligand, N73 with excellent IC_{50} value (6.7 nM).

2.2.10 Induced fit docking

The induced fit docking (IFD) [78] was applied by using Glide, Maestro, a mixed molecular docking and dynamics method where the receptor was flexible and ligand was rigid during the docking study. All the hits were prepared by the OPLS_2005 force field utilizing the LigPrep in Maestro. The hits were docked to the rigid protein using the Glide with van der Waals (vdW) radii scaling of 0.5 for the proteins and ligand nonpolar atoms [79]. The energy minimization was carried out on the 4XCT protein structure using force field OPLS_2005 with an implicit solvation model. The Glide XP mode was utilized for the initial docking using zinc as metal constraints atom, and 20 ligand poses were retained for protein structural refinement. The Prime (Schrödinger, LLC, New York, NY, 2015) was used to develop the induced-fit protein-ligand complexes. Each of the 20 structures from the previous step, were subjected to side-chain and backbone refinements [79]. All the residues, with at least one atom located within 5.0Å of each corresponding ligand pose, were included in the Prime refinement.

The refined complexes were ranked by Prime energy, and the protein structures within 30 kcal mol^{-1} of the minimum energy structure were put through the final round of Glide docking and scoring. Each ligand was docked into every refined low-energy protein structure using Glide XP. The resulting 20 new protein conformations were taken for docking using default Glide docking parameters. The binding affinity of each protein-ligand complex was reported in the Glide score. The higher negative Glide score indicated more favorable binding with MMP-9.

2.2.11 Prime MM-GBSA simulation

The free binding energies of the high scoring docked complexes were computed by utilizing the molecular mechanic-generalized Born surface area (MM-GBSA) followed by default parameters [80]. Du *et al.* developed the correlation model between the docking scores and calculated MM-GBSA binding-free energy with the experimental pIC_{50} values [81]. The Prime MM-GBSA simulations were carried out using the input complex structures from the IFD. The Prime in Maestro was employed to minimize the energy of the docked complexes. The OPLS_2005 force field in conjunction with GBSA continuum model [82] was utilized to determine the energies of the selected complexes of ligands. The binding free energies (ΔG_{bind}) of ligands were calculated using the equations [83].

$$\Delta G_{bind} = \Delta E_{MM} + \Delta G_{Solv} + \Delta G_{SA} \quad \ldots\ldots\ldots\ldots \quad (2.3)$$

$$\Delta E = E_{complex} - E_{protein} - E_{ligand} \quad \ldots\ldots\ldots\ldots (2.4)$$

where ΔE_{MM} is the difference between minimized energies of the MMP-9-inhibitor complex and sum of the minimized energies of unliganded MMP-9 and its inhibitor, ΔG_{solv} is the difference between GBSA solvation energies of enzyme-inhibitor complex and sum of the GBSA solvation energies of unliganded MMP-9 and inhibitor, and ΔG_{SA}

is the difference between surface area energies of the complex and sum of the surface area of unliganded enzyme and its inhibitor.

2.2.12 Docking using AutoDock

The selected hits, as MMP-9 inhibitors were docked by utilizing AutoDock Tools-1.5.6 and AutoDock 4.2 suite for the comparative study of the Glide XP docking, IFD, and AutoDock results. The crystal structure, 4XCT, was prepared using AutoDock Tools. Atom charges, solvation parameters, and polar hydrogens were added to the protein for docking simulation before converting to PDBQT file format. The ligands were drawn with Chem3D 16.0 chemical structure drawing software to obtain standard 3D structures and energies of the molecules were minimized using MM2 energy minimization method to carry out the docking simulation [84]. The ligand optimization was performed using the AutoDock 4.2, Gasteiger charges optimization, non-polar hydrogens were merged, and saved as PDBQT file. AutoDock requires pre-calculated grid maps, and the grid must surround the region of the active site of MMP-9. Therefore, the grid box was centered at the region including Gly186, Leu188, Ala189, Ala191, Glu227, His230, His236, Leu243, Tyr245, Met247, Tyr248, and His266 amino acid residues, and Zn302 that surrounded the active site. The grid box size was set at 40, 42, and 48 Å for x, y and z respectively, and the grid center was set to 20.683, −16.615, 19.006 for x, y and z respectively covering the active pocket. AutoGrid 4.0 was used to produce a grid with 0.375 Å spacing between grid points. The Lamarckian Genetic Algorithm (LGA) was used to search the best conformers and a maximum of 50 conformers was considered for each compound with the default setting. The Discovery Studio Visualizer is used for visualization of interactions. AutoDock Tools provided various methods to analyze the results of docking simulations, *viz.* conformational

similarity, visualizing the binding site and its energy, intermolecular energy and inhibition constant.

2.2.13 Prediction of ADME

The QikProp program in Maestro was utilized to predict the ADME properties (physiochemically significant and pharmaceutically applicable descriptors) of the compounds [85]. The QikProp was unable to neutralize the compounds and generate the descriptors in the normal mode. Therefore, the neutralization of all molecules was essential before performing QikProp. The QikProp predicted 44 properties for the compounds including principal descriptors, physiochemical properties as well as log P (octanol/water), QP%, log HERG, Caco-2 cell membrane permeability, MDCK cell permeability, and Lipinski'sruleoffive, which were crucial for rational drug design [86, 87].

2.2.14 Density functional theory

Density functional theory (DFT) is applied to study of the enzyme active sites, and in the determination and validation of enzymatic reaction mechanisms. In MMPs, the electronic structure of the zinc metal atom is responsible for the lion's share of the catalytic process and to adequately represent the reactions taking place at the enzyme's active site [88]. Electronic effects of drug-like molecules play significant role in the pharmacological effects [89]. Therefore, the most and least active inhibitors of the training set were optimized along with one of the final hits in Jaguar v8.7 (Schrödinger, LLC, New York, NY, 2015) program using Becke's three-parameter exchange potential and Lee-Yang-Parr correlation functional (B3LYP) theory [90, 91] with 6-31G* basis set. The molecular orbital surfaces, atomic electrostatics potential charges (EPS) and molecular electrostatic potential (MESP) were observed to compute the HOMO and LUMO. The HOMO energy proposes the region of small molecules, which can donate

electron during the complex formation, while LUMO energy manifests the capacity of the molecule to accept the electrons from the protein. The difference in HOMO and LUMO energy, known as HOMO-LUMO gap energy, indicates the electronic excitation energy [92] that is necessary to compute the molecular reactivity and stability of the ligand-protein complex [93].

2.2.15 *In silico* MMP-9 selectivity determination

The XP docking of final 24 hits was performed using crystal structure 4XCT, 3AYU, and 1HY7 for MMP-9, MMP-2, and MMP-3 respectively, to determine the selective binding affinity of hits towards MMP-9. The Glide in Maestro was utilized to perform Glide XP docking using the default setting for all docking steps with metal and metal coordination constraints.

2.2.16 *In vitro* MMP-9 enzyme inhibition

Four hits *viz.* H-2, H-5, H-9, and H-13 (ZINC06455433, ZINC09613137, ZINC21212924, and ZINC23114578) out of searched MMP-9 inhibitors were selected on the basis of Glide docking score, AutoDock energy, MMP-9 selectivity, and ADME properties. These hits, chemically known as 2-[4-(1,3-benzothiazol-2-yl)phenoxy]-N-(4H-1,2,4-triazol-3-yl)acetamide; N-[(1S)-1-(1H-1,3-benzodiazol-2-yl)-2-phenylethyl]-2-(1,4-dioxo-1,2,3,4-tetrahydro phthalazin-2-yl)acetamide; 2-[4-(phenylamino)phen oxy] -N-(1,3,4-thiadiazol-2-yl)acetamide; and 5-({[4-(4-ethylphenyl)-1,3-thiazol-2-yl] amino}methylidene)-2-sulfanylidene-1,3-diazinane-4,6-dione respectively, were purched from MolPort SIA, Riga, Latvia (MolPort id: MolPort-003-999-396, MolPort-004-040-871, MolPort-019-645-129, and MolPort-005-284-219 respectively).

Human MMP-9 fluorometric drug discovery kit, RED (CAS No. BML-AK306) was purchased from Enzo Life Sciences. Eight varying final concentrations (0.03−100 μM) of compounds were applied to a black well plate for the enzyme inhibition studies. The

enzyme MMP-9 at a final concentration of 9 mU/μL was added to each well plate and incubated in the dark for 1h at 37 °C. Then, the final concentration of 0.5 μM fluorogenic substrate was added in the incubated enzyme-inhibitor mixture. All the dilutions were made by fluorogenic assay buffer (pH 7.4). Continuous fluorescence reading with 1 min interval for 10 min of the plate was taken on Synergy H1 microplate reader (BioTek, USA) in excitation and emission modes at 545 and 576 nm. The assays were carried out in triplicate with a sample containing 0.5 μM of final substrate concentration for calibration, buffer as blank, control without inhibitor N-Isobutyl-N-(4-methoxyphenyl sulfonyl) glycyl hydroxamic acid (NNGH) and inhibitor NNGH. The activity was expressed in relative fluorescent units (RFU), and control was used to calculate the percentage inhibition. The data was processed, and IC_{50} values were calculated by using GraphPad Prism 5.0, GraphPad Software Inc.

2.2.17 *In vitro* AChE and BuChE enzyme inhibition

The AChE and BuChE inhibition studies were performed by using Ellman *et al.* method [72]. The four selected hit molecules (ZINC06455433, ZINC09613137, ZINC21212924, and ZINC23114578) out of ten were purchased from MolPort SIA, Riga, Latvia (MolPort-003-999-396, MolPort-004-040-871, MolPort-019-645-129, and MolPort-005-284-219 respectively). The AChE from *Electrophorus electricus* and BuChE from horse serum (lyophilized powder) (CAS No.9000-81-1, CAS No.9001-08-5, respectively) were purchased from Sigma Aldrich, India. Acetylthiocholine iodide (ATCI), butyrylthiocholine iodide (BTCI), 5,5´-dithio-bis(2-nitrobenzoic acid) (DTNB-Ellman's reagent) and phosphate buffer saline (PBS), pH 7.4 were procured from HiMedia Laboratories, India, and donepezil (Sigma Aldrich, India) was used as reference. The six different concentrations (75, 15, 7.5, 3, 0.6, and 0.12 μM) of hits, 0.25 mM DTNB, 0.06 U mL^{-1} of AChE or BuChE were combined in PBS and

incubated at 37 °C for 30 min to determine inhibition of AChE or BuChE. 0.36 mM of the substrate (ATCI or BTCI) was added to the reaction mixture before measuring the absorbance at 415 nm wavelength by Synergy HTX multi-mode reader (BioTek, USA). The process was performed in triplicate with a blank and control, to calculate the percentage inhibition due to the presence of selected hits. The IC_{50} values, *i.e.*, the concentration of the drug resulting in 50% inhibition of the enzyme activity, were determined graphically from inhibition curves (log inhibitor concentration vs. percent inhibition) utilizing GraphPad Prism 5.0, GraphPad Software Inc. [73].

The enzyme kinetic (the mechanism of inhibition by ligands) of AChE were determined by the previously described method [72]. Eight concentrations of substrate (ATCI; 0.1–1.15 μM) were incubated with AChE in the absence and presence of different concentrations of test molecules (0.25, 0.5 & 1 μM for ZINC06455433, ZINC09613137, and ZINC23114578; and 0.125, 0.25 & 0.5 μM for ZINC21212924). The absorbance was measured for 30 min at intervals of 5 min at 415 nm wavelength. The products formed during the time frame of 30 min were estimated by Beer-Lambert law. V_{max} and K_m values of Michaelis−Menten kinetics were computed by nonlinear regression from the substrate-velocity curves using GraphPad Prism 5. Linear regression was used to calculate inhibition constant (ki) utilizing Lineweaver-Burk plots [94]. Ki value was determined by the Yonetani-Theorell method in which the lines from the double reciprocal Lineweaver-Burk plot was extrapolated to intersect at a point [95]. The positive reciprocal x-values of intersecting point were the determined Ki value of hits. The kinetic enzyme assay was performed in triplicate.

2.2.18 Assay of propidium iodide displacement

The molecular modeling studies illustrated that selected hits were PAS selective AChE inhibitors. Propidium iodide is a specific PAS selective ligand, which displays 10-fold

fluorescence enrichment when bound to AChE. Its displacement by hits is the measurement of their affinity towards the PAS of AChE. The three concentrations (0.24, 1.0, and 3.0 μM) of test compounds, 5 μM AChE from electric eel (eeAChE) in PBS, pH 7.4, were added in black 96-well plates and were kept at room temperature for 6 h [96]. The sample solutions were incubated for 15 min with 20 μM of propidium iodide (HiMedia, India), and the intensity of fluorescence was measured in excitation and emission mode at 485 and 620 nm, respectively. The assay was carried out in triplicate.

2.2.19 *In vitro* blood-brain barrier permeation assay

The possible *in vitro* blood-brain barrier (BBB) permeation of compounds was determined by parallel artificial membrane permeation assay (PAMPA) as described by Di L. *et al.* [97, 98]. The donor microplates (PVDF membrane, pore size 0.45 μm) and acceptor microplates were obtained from Millipore, Bengaluru, India. The filter surface of donor microplate was impregnated with 4 μL of 20 mg mL^{-1} porcine brain lipid (Avanti polar lipids, Alabaster) in dodecane (Avra Synthesis, Hyderabad, India), and the acceptor microplates were filled with 200 μL of phosphate buffer saline (PBS, HiMedia Laboratories, India), pH 7.4. Test compounds of 5 mg mL^{-1} concentration were prepared in DMSO and diluted with PBS to obtain a final concentration of 100 μg mL^{-1}. The donor well plates were filled with 200 μL of the test solution and were carefully placed on the acceptor plate like a sandwich, carrying it undisturbed for 18h at 25 °C. The donor plates were then removed, and the concentration of compounds in the acceptor, and donor wells were determined by measuring absorbance. Each well was analyzed at five different wavelengths with three independent performances, and results were explicit as mean±SEM. The nine commercial drugs with known BBB permeability (verapamil, diazepam, progesterone, atenolol, dopamine, lomefloxacin, alprazolam,

chlorpromazine, and oxazepam) were utilized to validate the PAMPA model. The above-described method was followed to determine the experimental permeability, Pe(exp) values of drugs, and data were regressed against Pe(ref) from literature to establish a linear correlation [99].

2.2.20 Determination of cellular cytotoxicity and neuroprotection

2.2.20.1 Neuronal cell line cultures

The human neuroblastoma SH-SY5Y cell line was procured from National Centre for Cell Science (NCCS) Pune, India. Cells were cultured into T25 flasks containing Dulbecco's modified Eagle's medium nutrient mixture F-12 (DMEM-F12), supplemented with 10% fetal bovine serum (FBS), 1μM glutamine, 50 U mL^{-1} penicillin, and 50 μg mL^{-1} streptomycin and were maintained at 37 °C in 5% CO_2 humidified air. SH-SY5Y cells were subcultured in 96-well plates at a seeding density of 5×10^4 cells per well for MTT assay and neuroprotection study.

2.2.20.2 Determination of cell viability and neuroprotection

The MTT (3-(4,5-dimethyl thiazol-2-yl)-2,5-diphenyltetrazolium bromide) assay was performed to determine the cytotoxicity of selected hits [100]. After 24h incubation at 37 °C, the medium was changed with test compounds having concentrations of 50 μM and 100 μM, for another 24h at previously described conditions. 5 mg mL^{-1} of MTT (Sigma-Aldrich, India) in PBS was added to the culture medium and incubated for 4h at 37 °C. The medium was removed, and the blue formazan crystals formed were dissolved in DMSO and evaluated by measuring absorbance at 570 nm. The test was carried out in triplicate, and results were explicit as mean ± SEM.

Neuroprotectivity of selected hits was determined by evaluating their ability to protect SH-SY5Y cells against induced apoptosis by L-glutamate excitotoxicity. L-glutamate triggered amyloid beta (Aβ) neurotoxicity in SH-SY5Y cell line [101]. The cells were

treated with test compounds, at 25 μM concentration, and incubated for 2h. After incubation, cells were treated with a medium containing 100 μM of L-glutamate and left for an additional 24h. The cell viability, after the treatment of L-glutamate, was assessed by MTT assay. The medium was further replaced with 80 μL of fresh medium and 20 μL of MTT (0.5 $mg.mL^{-1}$) in PBS. After 4 h of incubation, the MTT solution was removed, and the crystals of formazan were dissolved in DMSO to measure the absorbance at 570 nm. Percentage of neuronal cell protection against L-glutamate was calculated by considering the absorbance of the control cells as 100% of the cell viability.

2.2.21 Molecular dynamics simulation

Molecular dynamics (MD) simulations is a computer simulation method for studying the physical movements of atoms and molecules in a biophysical system. The trajectories of atoms and molecules are resolved by numerically solved Newton's equations of motion for a system of interacting particles, where forces within the particles and their potential energies are often calculated by using interatomic potentials or molecular mechanics (MM) force fields [102]. MD simulations of the docked complex of ZINC21212924 and cocrystal ligand (N73) with 4XCT were performed by using Desmond with the OPLS_2005 force field [28, 103, 104]. The protein-ligand docked complex (.pv file) from XP docking, was taken for salvation by applying open TIP3P (transferable intermolecular potential with 3 points) water model in an orthorhombic box of dimension 20 × 20 × 20 Å [105]. The protein-ligand complexes had 12 overall negative charges, but 4NFN with crystal ligand had total 13 negative charges and was neutralized by adding Na^+ counter ion for simulation.

After completing system builder panel, the ligand-protein complex was minimized by steepest descent procedure, followed by BFGS (Broyden-Fletcher-Goldfarb-Shanno)

algorithm with threshold of 2.0 kcal mol^{-1} and 41667 iterations. The long-range electrostatic interactions, with a grid spacing of 0.8, were calculated by Ewald method (PME) [106]. Nose-Hoover thermostats maintained constant simulation temperature [107], and the pressure was controlled Martina-Tobias-Klein method [108]. The cut-off distance between 8.0 to 12.0Å was applied to compute van der Waals and short-range electrostatic interactions using a truncated and force-shift manner termed as Shifted Force Lennared-Jones (SFLJ) [109], and cut-off 9.0Å gave best simulations results [110]. MD simulations were performed at 300K temperature and 1.01325 bar pressure. The multistep RESPA integrator [111], with an internal time step of 2.0 fs for bonded interactions and non-bonded interactions within 6.0 fs cut-off, was used to integrate the equations of motion. The overall model system was relaxed for 2 ns, before a 50 ns simulation. The default relaxation processes for NPT ensemble were executed in the following steps. The complex was minimized first with restrained solute and without solute. It was simulated in NVT ensemble using a Berendsen thermostat with simulation time of 12 ps at 10K temperature, constant fast temperature relaxation and velocity resampling every 1ps under restrained non-hydrogen solute atoms. After that, it was simulated in NPT ensemble using Berendsen thermostat and Berendsen barostat with simulation time of 12 ps at 10K temperature and 1 atm pressure with constant fast temperature and continuous slow pressure relaxation. The resampling velocity was at every 1 ps under restrained non-hydrogen solute atoms. Further simulation in NPT ensemble was undertaken with simulation time of 24 ps, at 300K temperature and 1 atm pressure under constant fast temperature and continuous slow pressure relaxation with resampling velocity at every 1 ps under restrained non-hydrogen solute atoms. The final relaxation in NPT ensemble was carried out in simulation time of 24 ps at 300K

temperature and 1 atm pressure under fast constant temperature, and normal constant pressure.

Coulombic interactions were characterized by short-range cut-off radius of 9.0Å, and long-range smooth particle mesh Ewald tolerance of 1×10^{-9}. Recording interval of 1.2 ps was defined for energy calculations and trajectory analyses. The performance of first seven steps of molecular simulations to relax the model system, before final simulations were performed. First step was to recognize traits of system and create a mature model system for regular MD. Second was simulated Brownian Dynamics NVT at temperature 10 K with small timesteps and restraints on heavy solute atoms for 100 ps. Third stage was simulated NVT at 10K, following small timesteps and restraints on heavy solute atoms during 12 ps. Fourth was simulated NPT at 10K and restraints on solute heavy atoms for 12 ps. Fifth stage was detecting solvate pocket(s). Sixth step was simulation NPT with restraints on solute heavy atoms during 12 ps, and seventh was simulated at NPT and no restraints for 24 ps. Results of MD trajectories were analyzed, and figures regarding MD simulation of protein-ligand complex were collected after final 50 ns.

2.3 Results and Discussion

2.3.1 Energetically optimized structure-based pharmacophore generation

2.3.1.1 Preparation of protein

The X-ray crystallographic structures of MMP-9, with low resolution and cocrystals with highly specific MMP-9 inhibitory activity, were obtained from the PDB database. Five crystal structures with resolution between 1.65Å and 2.90Å and potent MMP-9 inhibitory activity (IC_{50} range from ≤0.4 to 6.0 nM and Ki 21 nM) were taken for developing e-pharmacophore. Out of these, four PDB structures (4XCT, 4WZV, 2OVX, and 2OW2) represent cocrystal inhibitors containing a hydroxamate group, while the

fifth (1GKC) represents cocrystal inhibitor of reverse hydroxamate (**Figure 2.2)**. Protein preparation wizard was used to prepare these proteins utilizing default settings with OPLS_2005 force field. The final refinement protein structures are sketched in **Figure 2.4**.

The five refined cocrystal ligands were docked onto the respective prepared protein structures to develop e-pharmacophore. The root-mean-square deviation (rmsd) of all five cocrystal ligands were less than 1Å. The ligand interaction with MMP-9 crystal structures revealed as Leu188, Ala189, and Try423 the essential residues. In the refined 4XCT structure, Leu188, Ala189, and Glu227 generated hydrogen-bonding interaction, His226, Pi-Pi stacking interaction and Zn302, a salt-bridge with cocrystal ligand. Further, Leu188, Ala189, and Ala191 of 4WZV PDB structure produced hydrogen-bonding interaction and His226 and His230, Pi-Pi stacking and Zn302, salt-bridge with cocrystal ligand. However, within the refined 2OVX and 2OW1 crystal structures, Leu188 and Ala189 were interacting through hydrogen-bonding, His401 and Tyr423 by Pi-Pi stacking and Zn444 by salt-bridge with cocrystal ligand. In the refined 1GKC crystal structure, Gly186, Leu188, Glh402, Pro421, and Tyr423 were interacting mainly through hydrogen-bonding and Zn1450 by salt-bridge with cocrystal ligand.

2.3.1.2 Generation of energy-based pharmacophore

The different aspects of structure-based and ligand-based techniques combined with an e-pharmacophore method explored five crystal structures of MMP-9 and were used in the study. The e-pharmacophore hypotheses were generated by mapping Glide XP energetic terms onto pharmacophore sites, which were calculated by the structural and energy information between the protein and the ligand. The number of pharmacophore sites was set up to 10 initially for all of the crystal structures. The pharmacophore hypotheses were generated from Glide XP energies score onto pharmacophoric sites.

The hypotheses were also considered with higher pharmacophoric sites and lesser energetic scores from each MMP-9 crystal structure. The selected e-pharmacophores with the distance between the features are presented in **Figure 2.5**. Total number of pharmacophore sites for each ligand before energy-based site selection, were optimized for hypothesis generation for all the five crystal structures. The selected hypotheses are given in **Table 2.2**. The distances between the pharmacophore features of energy-based pharmacophores are included in **Table 2.3**.

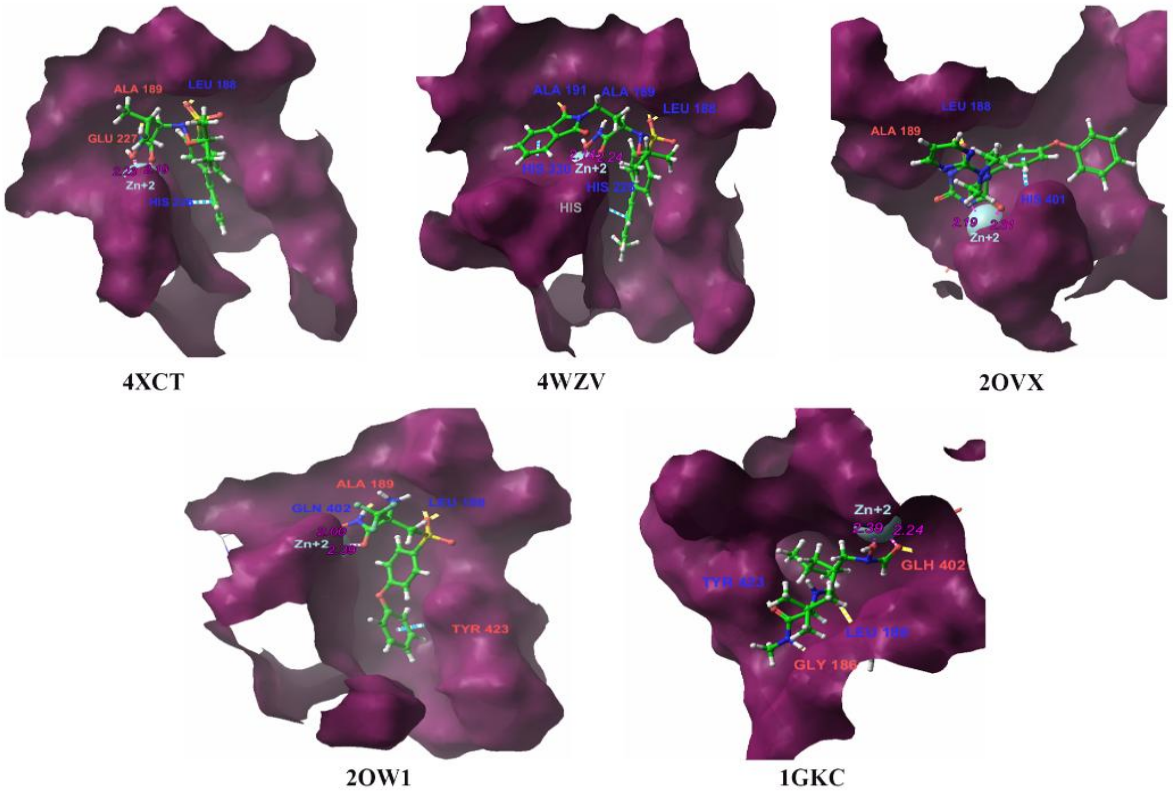

Figure 2.4 MMP-9 binding site pockets (maroon) with cocrystal ligands (green) from five PDB codes, utilizing "create binding site surfaces."

2.3.2 Validation of e-pharmacophore model

The enrichment factor, goodness of hit score, Boltzmann-enhanced discrimination of receiver operating characteristic, receiver operating characteristic curve value, robust initial enhancement, and area under accumulation curve were evaluated to validate e-pharmacophore model. The decoy set of 1090 compounds consisting of 90 known

inhibitors, which were not utilized in the pharmacophore hypothesis building, were used for validation of hypotheses.

Table 2.2 e-Pharmacophore hypotheses with feature scores

PDB id	No. of possible site	No. of selected site	Hypothesis*	Feature score*
4XCT	6	4	DDRR	D6:−1.00; D7:−0.66; R10:−1.02; R11:−1.66
4WZV	6	5	ADDRR	A3:−0.52; D7:−0.67; R11:−1.31; R12:−1.42
2OVX	7	4	ADRR	A3:−0.52; D7:−0.67; R11:−1.31; R12:−1.42
2OW1	5	4	DNRR	D5:−0.32; N7:−6.55; R9:−1.45; R10:−1.22
1GKC	5	4	AADD	A3:−0.70; A4:−0.36; D6:−0.70; D7:−0.70

*A, Hydrogen-bond acceptor; R, Aromatic ring; D, Hydrogen-bond donor; N, Negative ionizable group.

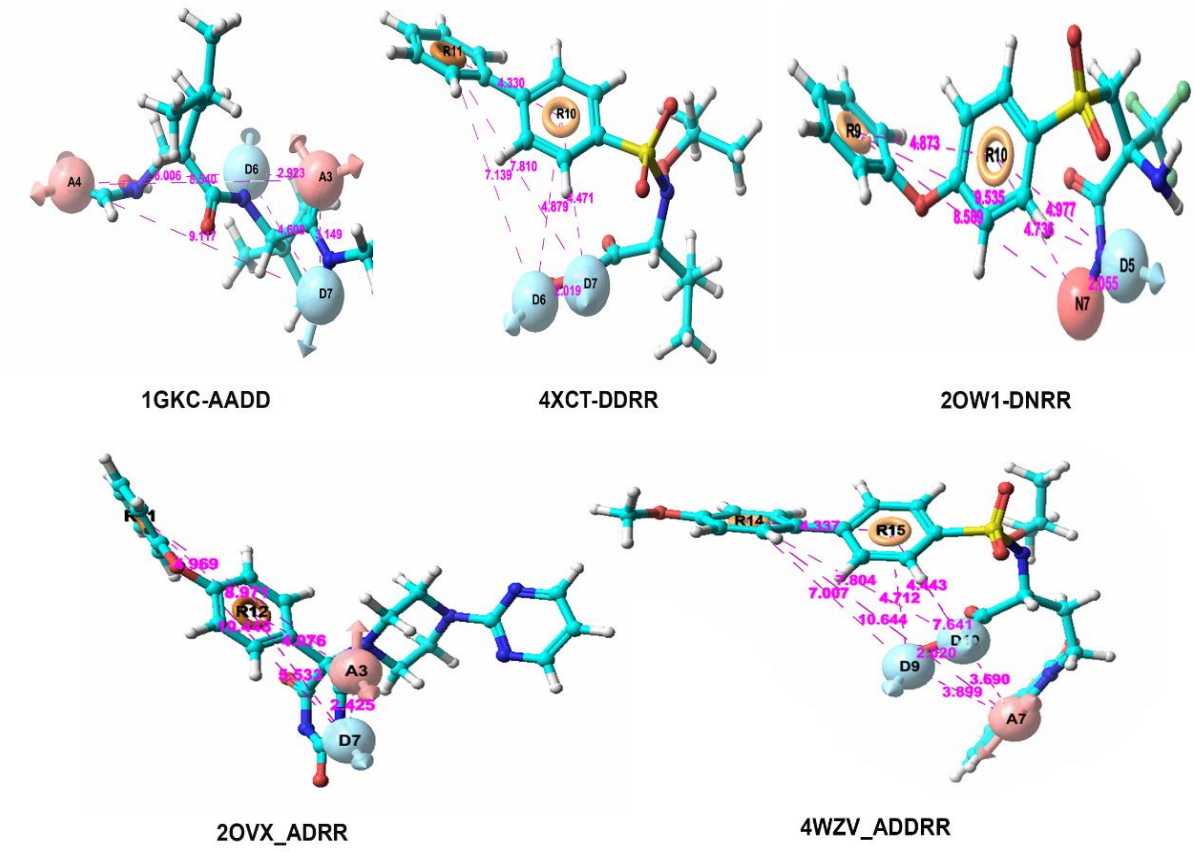

Figure 2.5 e-Pharmacophore hypotheses with their respective PDB codes. A, hydrogen-bond acceptor, pink sphere with arrow; R, aromatic ring, yellow open circle; D, hydrogen-bond donor, blue sphere with the arrow; N, negative ionizable group, pink sphere.

The Güner-Henry scoring method was used to validate the developed e-pharmacophore models. The ROC plots for all the selected hypotheses were generated, and the AUAC was used as a measure of accuracy. The significant values of enrichment factors, *viz*. 1.003, 1.043, 1.042, 0.961, 1.020; GH scores *viz.* 0.561, 0.596, 0.588, 0.475, 0.565; and AUAC ≥0.7 were produced by e-pharmacophores. The values of parameters indicated that all five pharmacophores were suitable for pharmacophore-based virtual screening (**Table 2.4**).

Table 2.3 Distance between the pharmacophore features of e-pharmacophores

Hypothesis*	**Distance from A to A (Å)**	**Distance from A to D (Å)**	**Distance from A to R (Å)**	**Distance from D to D (Å)**	**Distance from D to R (Å)**	**Distance from D to N (Å)**	**Distance from N to R (Å)**	**Distance from R to R (Å)**
4XCT-DDRR				2.019	4.879; 4.471; 7.139; 7.810			4.33
4WZV-ADDRR		3.899; 3.690	7.641; 10.644	2.020	4.712; 7.007; 7.804; 4.443			4.337
2OVX-ADRR		2.425	8.971; 4.076		10.448; 5.533			4.969
2OW1-DNRR					9.535; 4.977	2.055	8.589; 4.736	4.873
1GKC-AADD	8.540	2.923; 3.149; 6.006; 9.117		4.608				

*A, H-bond acceptor; D, H-bond donor; R, aromatic ring; N, negative ionic group.

2.3.3 Development of ligand-based pharmacophore model

The ligand-based pharmacophore modeling (3D-QSAR) using PHASE developed two types of 3D-QSAR models: Atom-based (where all atoms of ligand were taken for model development), and pharmacophore-based (where the pharmacophore sites of the molecule matched to the hypothesis). The dataset of 155 MMP-9 inhibitors was divided into actives, inactives, and moderately actives and was selected for Atom-based 3D-QSAR model development. First, the conformers were developed and checked for the

effect of different partial charges. The pharmacophore sites were then created, and the common pharmacophores of selected MMP-9 inhibitors were identified by utilizing PHASE. The PHASE generated total of 258 hypotheses and scored them. The top three pharmacophore hypotheses were considered (**Table 2.5**) on the basis of good survival activity, vector scores, volume scores, energy scores, best active alignment, and the number of site matches.

Table 2.4 Evaluation of e-pharmacophores utilizing enrichment calculation

Parameter	**4XCT**	**4WZV**	**2OVX**	**2OW1**	**1GKC**
Total molecules in the database (D)	1090	1090	1090	1090	1090
Total actives in the database (A)	90	90	90	90	90
Total Hits (Ht)	164	152	152	157	157
Active Hits (Ha)	83	83	82	69	81
True negatives	1000	1000	1000	1000	1000
False negatives (A-Ha)	7	7	8	21	9
False positives (Ht-Ha)	919	881	871	801	881
% Yield of actives [(Ha/Ht)×100]	8.28	8.61	8.60	7.93	8.42
% Ratio of actives [(Ha/A)×100]	92.22	92.22	91.11	76.67	90.00
Enrichment factor (EF)	1.003	1.043	1.042	0.961	1.020
Goodness of hit score (GH)	0.561	0.596	0.588	0.475	0.565
BEDROC (α= 160.9)[a]	0.648	0.718	0.626	0.611	0.608
BEDROC (α= 20.0)	0.291	0.367	0.383	0.332	0.312
BEDROC (α= 8.0)	0.338	0.387	0.413	0.355	0.351
ROC[b]	0.70	0.71	0.73	0.82	0.72
RIE[c]	2.84	3.59	3.75	3.25	3.05
AUAC[d]	0.69	0.70	0.71	0.80	0.70
EF(1%)[e]	2.1	2.0	2.4	1.8	1.9

[a]Boltzmann-enhanced discrimination of receiver operating characteristic, [b]Receiver operating characteristic curve value, [c]Robust initial enhancement, [d]Area under accumulation curve, [e]Enrichment factor at 1% of the decoy data set.

Hypothesis-1 (AAAHR) showed three hydrogen-bond acceptors, one hydrophobic group and one aromatic ring, hypothesis-2 (AAADR) showed three hydrogen-bond acceptors, one hydrogen-bond donor, and one aromatic ring, and hypothesis-3 (AADHR) had two hydrogen-bond acceptors, one hydrogen-bond donor, one

hydrophobic group and one aromatic ring as features. Among these, hypothesis-1 (AAAHR) produced highest survival score. The features of selected ligand-based hypotheses are presented in **Figure 2.6**. The distances between the pharmacophore features of ligand-based pharmacophores are listed in **Table 2.6**.

Table 2.5 Ligand-based hypotheses (3D-QSAR) with various scores

Hypothesis	Survival score	Survival-inactive score	Site score	Vector score	Volume score
AAAHR	3.463	1.754	0.82	0.983	0.656
AAADR	3.228	1.559	0.73	0.862	0.635
AADHR	3.088	1.858	0.6	0.87	0.621

Table 2.6 Distance between the pharmacophore features of ligand-based hypotheses

3D-QSAR*	Distance from A to A (Å)	Distance from A to D (Å)	Distance from A to R (Å)	Distance from D to R (Å)	Distance from A to H (Å)	Distance from D to H (Å)	Distance from H to R (Å)
AAAHR	2.540; 6.58; 6.599		2.781; 3.909; 3.919		6.481; 0.414; 10.835		8.010
AAADR	5.588; 6.563; 10.944	4.671; 8.125; 10.413	2.781; 3.893; 7.337	5.668			
AADHR	6.583	5.252; 5.655	2.781; 3.905	4.110	6.475; 10.746	11.634	8.289

*A, H-bond acceptor; D, H-bond donor; H, hydrophobic group, and R, aromatic ring.

2.3.4 Validation of 3D-QSAR models

The internal and external statistical validations of developed 3D-QSAR pharmacophore hypotheses were necessary for the accuracy of predictions. We randomly selected 124 compounds as training set and 31 as test set to generate the hypotheses. Statistically relevant parameters were obtained in favor of internal statistical validation by PLS analysis by the LOO method (**Table 2.7**). The three 3D-QSAR models, *i.e.*, hypothesis-1 (AADHR), hypothesis-2 (AAADR), and hypothesis-3 (AADHR) showed good predictivity, but hypothesis-3 showed better predictive ability than the other two (**Table 2.7**). Hypothesis-3 showed a good R^2 value of 0.957 and SD of 0.213 for the training

set, good predictive capability with Q^2 of 0.691, F value of 524.2, and r^2_{pred} of 0.696 for the test set. The correlation coefficient values of the training set (R^2) should be higher than 0.5; correlation coefficient value of predicted activities for test set (Q^2) should be higher than 0.5 to attain good predictivity. The standard deviation (SD) below 0.3, high value of variance ratio (F), and minimum root-mean-square error (RMSE) were the validation limits of selected 3D-QSAR model. The predictive correlation coefficient (r^2_{pred}) value generated by the test set also demonstrated the real predictive ability of the QSAR model. The correlation coefficient (R), high slope of regression lines through the origin (k and k′ values should be close to 1) and the related values of R_0^2 and the R'_0 were obtained by calculating the correlation coefficient of regression lines of the scatter plot (**Figure 2.7).**

Table 2.7 Internal validation parameters of 3D-QSAR models

Statistical parameter*	**AADHR**	**AAAHR**	**AAADR**
Number of molecules in training set	124	124	124
Number of molecules in test set	31	31	31
R^2	0.957	0.938	0.960
SD	0.213	0.246	0.209
Q^2	0.691	0.687	0.541
F-value	524.2	358.1	569.7
RMSE	0.518	0.600	0.562
Pearson-R	0.832	0.866	0.756

*R^2, The square of correlation coefficient; SD, Standard deviation of the regression; Q^2, Squared Q value for the predicted activities; F-value, Variance ratio; RMSE, Root-mean-square error; Pearson-R, Correlation between the predicted and observed activities for the test set.

The plot was obtained from actual activity versus predicted activity and predicted activity versus actual activity, characterized the best predictive capability of the models. The developed 3D-QSAR model from AADHR hypothesis afforded r^2_{cv} value of 0.903, a parameter of modified r^2 [$r_m^2{}_{(LOO)}$] was 0.813 (>0.5). The values of external validation

parameters (**Table 2.8**) of three models (AADHR, AAAHR, and AAADR) were above the limitations and proved that the models were statistically significant.

Table 2.8 External Statistical Validation of 3D-QSAR hypotheses

Validation parameter*	**AADHR**	**AAAHR**	**AAADR**	**Limit**
r^2_{cv}	0.903	0.879	0.901	$r^2_{cv} > 0.5$
r^2	0.902	0.880	0.902	Close to 1
k value	0.901	0.843	0.895	$0.85 \leq k \leq 1.15$
k´ value	0.999	0.998	0.995	$0.85 \leq k \leq 1.15$
R_0^2	0.903	0.881	0.902	Close to r^2
$R_0'^2$	0.893	0.851	0.891	Close to r^2
$R_{m}^{2}{}_{(LOO)}$	0.813	0.728	0.805	$R_{m}^{2}{}_{(LOO)} > 0.5$
R^2_{pred}	0.696	0.691	0.573	$R^2_{pred} > 0.5$

*r^2_{cv}, Cross-validated coefficient; r^2, Correlation coefficient between the actual and predicted values; k and k′ value, Slopes of regression lines; R_0^2 and $R_0'^2$, Correlation coefficients for the regression lines through the origin; $R_{m}^{2}{}_{(LOO)}$, Modified squared correlation coefficient using LOO method; R^2_{pred}, Predictive correlation coefficient value.

2.3.5 Analysis of contour maps

The AADHR hypothesis obtained from 3D-QSAR model was used to generate contour maps. These contour maps were necessary to identify the positions of the substitutions or replacements of atoms to increase biological activity. Visualizing and understanding of the maps against most active (48) and least active (36) inhibitors can help to identify the novel scaffolds with good activity. The contour maps were generated by utilizing most and least active MMP-9 inhibitors from the training dataset (**Figure 2.8**). The hydrogen-bond donor effect (**Figure 2.8A** and **B**), hydrophobic effect (**Figure 2.8C** and **D**) and electron-withdrawing nature (**Figure 2.8E** and **F**) of most active and least active inhibitors were sketched in contour map figure.

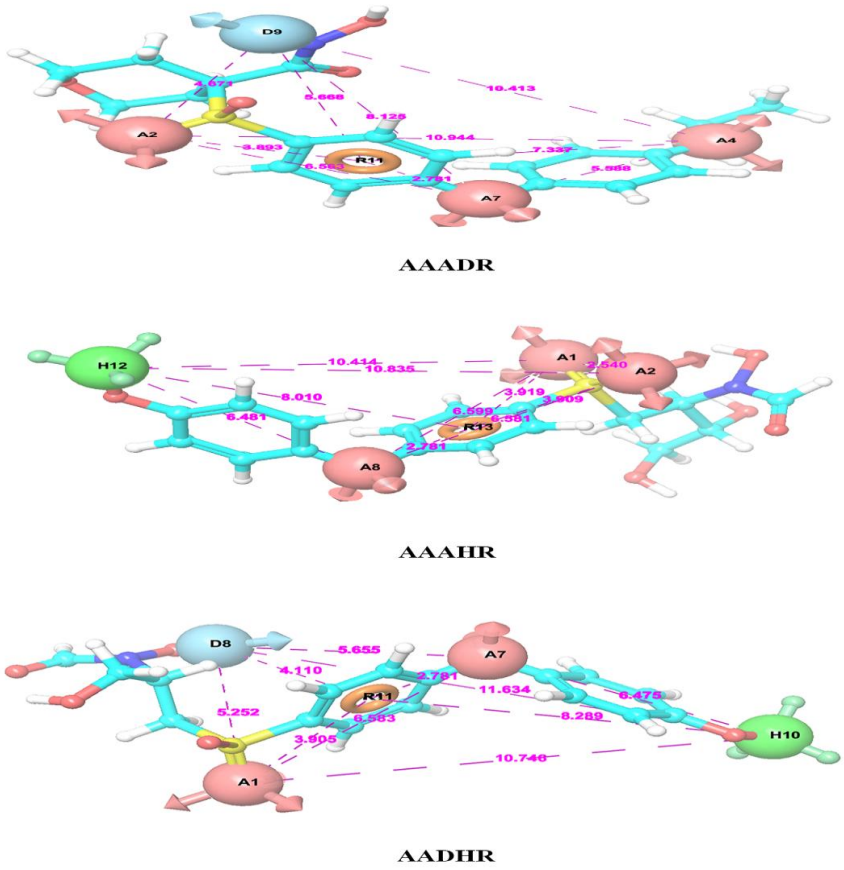

Figure 2.6 3D-QSAR based-pharmacophore hypotheses. A, hydrogen-bond acceptor, pink sphere with arrow; D, hydrogen-bond donor, blue sphere with arrow; R, aromatic ring, yellow open circle; H, hydrophobic group, green sphere.

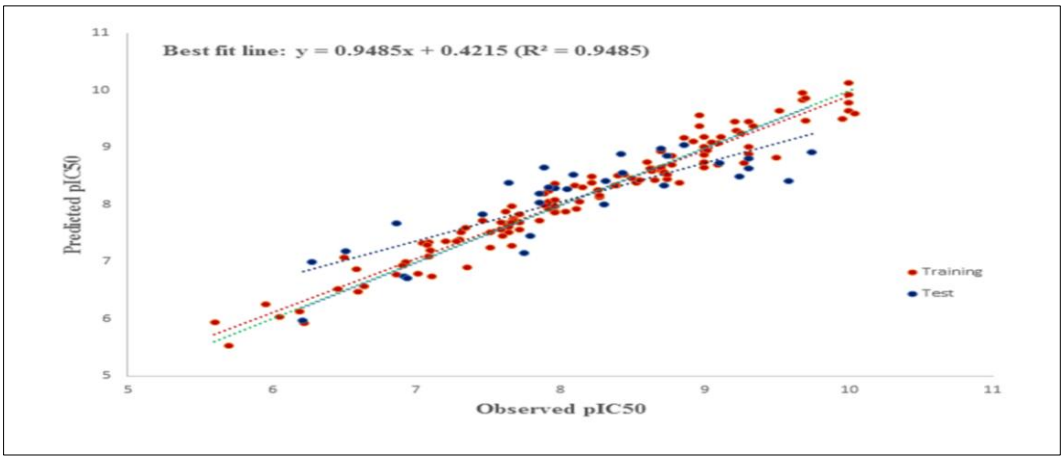

Figure 2.7 Plot of the observed pIC_{50} versus predicted pIC_{50} of MMP-9 inhibitors from the model AADHR obtained by using 124 training set ligands and validated by using 31 test set ligands. Red dot line represents regression line for the training set, blue dot line for test set and green dot line for training set of compounds when intercept set as zero. The equation is the best fit line of training set.

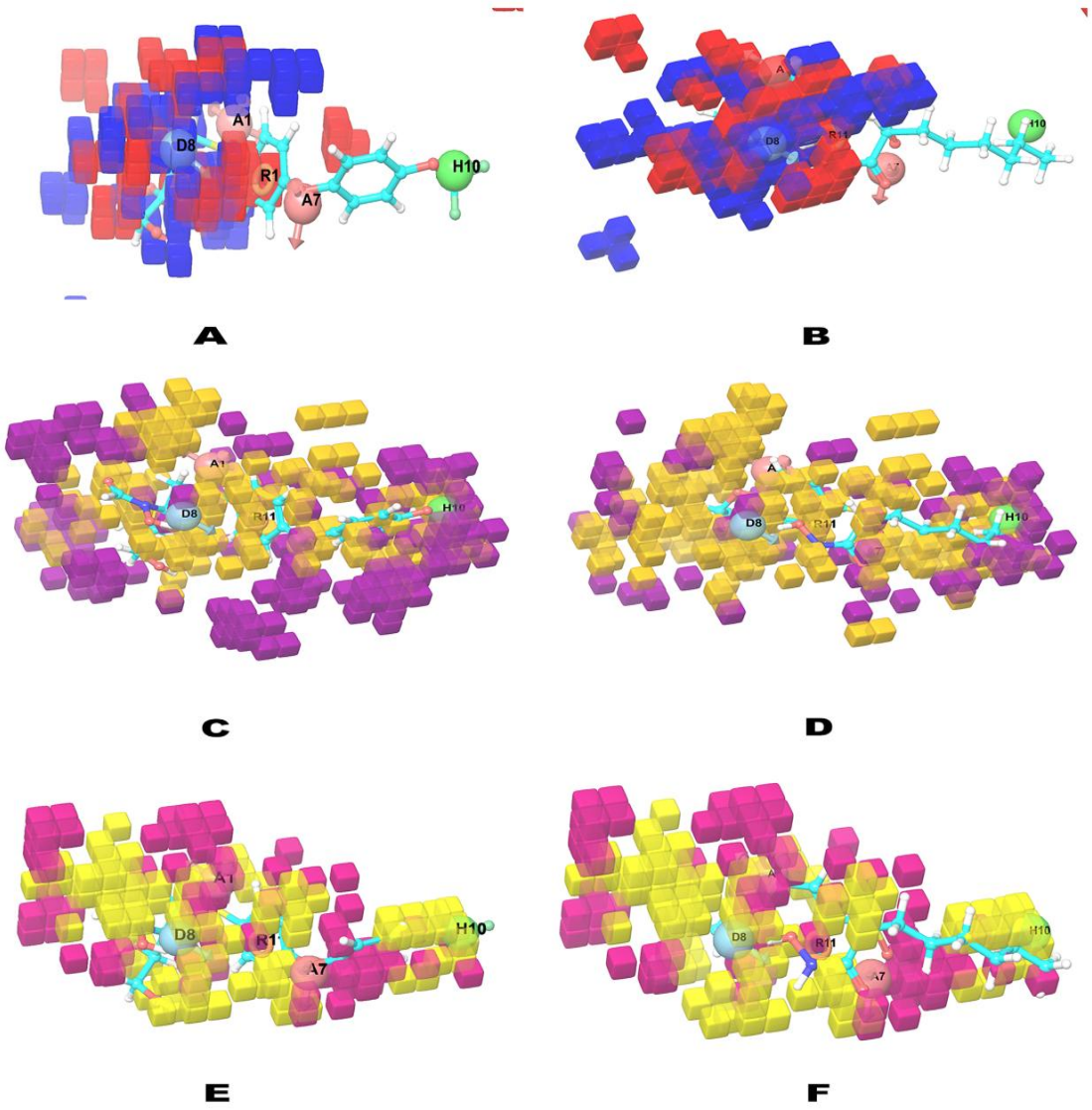

Figure 2.8 Contour maps of most active (left) and least active (right) known MMP-9 inhibitors. Hydrogen-bond donor effect, most active, A & least active, B (blue for favorable; red for unfavorable); non-polar effect, most active, C & least active, D (orange-yellow, favorable; purple, unfavorable); electron-withdrawing effect, most active, E; and least active, F (yellow, favorable; maroon, unfavorable).

2.3.6 Pharmacophore-based virtual screening, removal of PAINS and molecular docking

Pharmacophore-based virtual screening of the database is a favorite resource for the initial stage of hit identification. The fitness score is a measure of how well the ligand fits with the pharmacophore. The hits with high fitness scores were considered as very active inhibitors. All five e-pharmacophores and three ligand-based pharmacophores were utilized to screen the hits against Zinc15 database compounds. PAINs molecules

were removed before performing HTVS. The fitness score of more than 1.0 was taken as the limit for the Glide HTVS followed by Glide SP and XP docking. The number of hits retrieved from pharmacophore-based virtual screening is presented in **Table 2.9.** Molecular XP docking was performed for the 278 retrieves with the 4XCT crystal structure and twenty-four compounds with the best docking scores (−11.74 to −9.02 kcal mol^{-1}) and Glide energies (−72.31to −44.46 kcal mol^{-1}) were taken (**Table 2.10**) for further studies**.** The fitness scores, number of H-bonds, and interacting amino acids of hits with cocrystal ligand of 4XCT (N73) are shown in **Table 2.10**. The structures of 24 hits (Appendix; **Figure A.2)** and their 2d binding poses with the active site of MMP-9 are pictured (Appendix; **Figure A.3**, and **A.4**).

Table 2.9 Number of hits retrieved at each stage of pharmacophore-based (structure and ligand-based) virtual screening

Pharmacophore	PHASE find matches hits	HTVS hits	SP hits	XP hits	Final retrieves
DDRR	26000	22403	2599	239	25
ADDRR	8600	8352	873	77	8
ADRR	63700	60382	6396	579	63
DNRR	4212	3843	431	43	5
AADD	60060	59015	6027	489	63
AAADR	50156	43024	4364	363	43
AAAHR	5544	51038	5289	412	53
AADHR	20621	20196	2087	173	20

2.3.7 Induced fit docking

The results from induced-fit docking showed superior performance on both ligand binding pose and docking score accuracy of the rigid-receptor docking. The IFD docking score of final hits (**Table 2.11**) was very close to the Glide scores with little variations. Both Glide and the IFD protocols yielded Glide scores as −11.74 and −12.18 kcal mol^{-1}. The conformation generated from the IFD is slightly different from the docked pose produced from the rigid receptor docking. The Glide-based model afforded

an RMSD of 5.2Å, when compared to the native pose in the crystal structure. The IFD score of final 24 hits was excellent and between −342.78 to −333.83 kcal mol^{-1} (**Table 2.11**).

Table 2.10 Hits with their Zinc id, number of H-bonds, interacting amino acid residues, XP docking score, and Glide energy

Hit	Compound[a]	H-bond	Ligand interacting amino acid residues	XP docking score	Glide energy
H-1	ZINC12571902	3	Ala189[b], Glu227[b], Leu243, His226*	−11.74	−72.31
H-2	ZINC06455433	2	Ala191[b], Glu227[b], His226*, His236*	−11.12	−59.85
H-3	ZINC71958240	3	Ala189[b], Try245[b], Met247[b], His226*	−11.06	−68.41
H-4	ZINC72927088	1	Glu227[b], His226*	−11.05	−50.81
H-5	ZINC21212924	1	Tyr245[b], His226*, His230*, His236*	−10.37	−50.66
H-6	ZINC05110584	2	Gly186[b], Met247[b], His226*	−10.33	−52.03
H-7	ZINC72465895	2	Ala191[b], Glu227[b], His226*	−10.32	−57.99
H-8	ZINC92123812	1	Leu188[b], His226*	−10.11	−49.88
H-9	ZINC09613137	1	Pro246[b], His226*	−10.03	−48.99
H-10	ZINC94152976	0	His226*, Tyr248*	−9.98	−48.13
H-11	ZINC04317343	1	Tyr245[b], His226*	−9.78	−53.84
H-12	ZINC22261799	1	Ala189[b], His226*, Tyr248*	−9.71	−47.13
H-13	ZINC23114578	1	Leu188[b], His226*, Tyr248*	−9.67	−49.68
H-14	ZINC24153064	2	Ala189[b], His190[b], His226*	−9.52	−48.85
H-15	ZINC57681257	2	Ala189[b], His190[b], His226*	−9.43	−44.46
H-16	ZINC83304012	1	Tyr245	−9.41	−51.63
H-17	ZINC93244851	4	Leu188[b], Ala189[b], Glu227[b], Pro246[b], His226*	−9.39	−63.49
H-18	ZINC09502427	2	Ala189[b], His190[b], His226*	−9.38	−54.95
H-19	ZINC12778243	1	Leu188[b], His226*	−9.38	−53.94
H-20	ZINC10024450	2	Pro246[b], Tyr248[b], His226*	−9.25	−61.37
H-21	ZINC09592952	2	Leu188[b], Ala189[b], His226*, Tyr248*	−9.06	−50.57
H-22	ZINC08588140	1	His190[b], Phe192*, His226*	−9.03	−54.20
H-23	ZINC28624478	2	Glu227[b], Tyr245b	−9.02	−47.08
H-24	ZINC12527222	2	Ala189[b], Glu227[b], His226*, His230*, His236*	−9.02	−56.22
Cry[c]	N73	3	Ala189[b], Leu188[b], His226*, Tyr248*	−8.36	−49.99

[a]Compound code from ZINC database; [b]Residue showed H-bonding interaction; [c]Cocrystal ligand of crystal structure 4XCT; *Residue showed π-π stacking interaction.

2.3.8 Determination of Prime MM-GBSA

Multiple docking strategies and Prime MM-GBSA calculations were applied to predict the binding mode and binding free energy (ΔG_{bind}) for MMP-9-hits and MMP-9–N73 complexes. The hit molecules from the multiple docking studies (except H-12, H-14, H-15, H-19, H-23, H-24) displayed higher binding free energies, compared to cocrystal ligand of 4XCT, N73 (−66.71 kcal mol^{-1}) (**Table 2.11**). Among them, H-3 showed highest ΔG_{bind}, −102.0 kcal mol^{-1} and H-12 showed lowest ΔG_{bind}, −36.84 kcal mol^{-1}. The binding free energy determination based on Prime MM-GBSA method also supported the stability of hit-MMP-9 complexes.

2.3.9 AutoDock simulation

The AutoDock binding energy and inhibition constant (IC_{50}) for the possible interaction between MMP-9 and hits were calculated and presented in **Table 2.11**. The binding energy of final 24 molecules was between −10.04 to −12.75 kcal mol^{-1}. The predicted IC_{50} of cocrystal N73 was 3.4nM, and the actual value was 6.7 nM. The H-6, H-9, and H-20 showed picomolar inhibition constants, H-9 and H-20 were selective MMP-9 inhibitors. The prediction of results was strongly supported by the Glide XP docking and IFD results.

2.3.10 Prediction of ADME properties

Forty-four physicochemically significant descriptors and pharmaceutically relevant properties of 24 hits were evaluated to analyze their drug-likeness and pharmacokinetics including ADME. The QikProp tool in Maestro was utilized for evaluation of drug-like behavior through analysis of absorption, distribution, metabolism, and excretion (ADME) and other pharmacokinetic parameters (**Table 2.12**). All the hits showed good partition coefficient ($QPlogP_{o/w}$) values (from 2.374 to 4.543), which were essential for the absorption and distribution of drugs. QPPCaco, a predicted apparent Caco-2 cell

permeability in nm/s, was in the range of 1815.10 to 170.61. All the compounds passed the entire pharmacokinetic requirements for a drug-like molecule and were within the acceptable range for human use*. The overall percentage of human oral absorption was between 85.112 to 100.0, and water solubility (QPlog S) was between −4.128 to −7.822.

Table 2.11 Hits with their XP docking score, IFD scores, AutoDock binding energy, and AutoDock calculated enzyme inhibition constant results

Hit	IFD docking score	IFD score	AutoDock binding energy (kcal/mol)	Calculated inhibition constant (nM)	MM-GBSA-ΔG_{Bind}
H-1	−12.175	−337.89	−10.53	19.05	−68.66
H-2	−11.115	−339.01	−11.26	5.56	−88.25
H-3	−11.784	−340.55	−11.01	8.71	−102.0
H-4	−13.868	−342.78	−10.04	47.33	−91.46
H-5	−10.391	−338.34	−11.77	2.35	−66.91
H-6	−10.84	−341.49	−12.69	0.499	−73.83
H-7	−10.734	−337.71	−10.42	672.38	−84.83
H-8	−9.459	−335.27	−11.58	3.26	−75.71
H-9	−10.986	−338.62	−12.51	0.675	−67.77
H-10	−11.324	−338.34	−10.71	12.65	−92.76
H-11	−10.925	−338.99	−10.81	11.96	−76.98
H-12	−11.025	−338.6	−10.62	16.35	−36.84
H-13	−8.783	−336.00	−11.76	2.4	−86.98
H-14	−10.173	−338.34	−10.52	19.49	−61.54
H-15	−10.212	−338.63	−10.83	11.51	−66.56
H-16	−9.325	−333.83	−10.16	35.58	−69.25
H-17	−11.07	−337.13	−10.8	14.94	−85.95
H-18	−9.719	−339.37	−10.81	11.88	−75.29
H-19	−11.395	−340.13	−11.08	7.57	−61.78
H-20	−9.333	−338.23	−12.75	0.448	−97.45
H-21	−9.943	−333.84	−11.61	3.09	−76.73
H-22	−10.046	−337.56	−10.31	5.14	−88.46
H-23	−10.018	−338.88	−10.42	22.93	−65.59
H-24	−10.224	−339.29	−10.92	9.97	−45.42
N73	−7.752	−332.21	−11.51	3.4	−66.71

*log HERG values less than −5 were a concern & compounds could be weaker HERG blockers.

Other parameters, *i.e.*, molecular weight, H-bond donors, H-bond acceptors, and logP according to Lipinski's rule of five, were evaluated and found to be within the limit of

drug-likeness. The compounds with better binding affinity and good predicted pharmacokinetic properties were considered as hits (Appendix; **Figure A.2**).

Table 2.12 Physiochemical descriptors of hits calculated by Qikprop model

Hit*	Mol Wt[a]	QP log P(o/w)[b]	QP logS[c]	QP PCaco[d]	QP log HERG[e]	QP PMDCK[f]	% Human oral absorption[g]
H-1	438.54	4.507	−7.822	389.887	−7.028	393.024	100.0
H-2	351.38	2.842	−5.093	256.415	−6.702	182.444	86.7
H-3	442.88	3.202	−5.986	264.671	−6.676	408.44	89.1
H-4	363.24	4.262	−5.18	692.455	−7.159	2121.232	100.0
H-5	326.37	2.932	−4.684	479.518	−6.704	384.398	92.1
H-6	358.40	3.274	−5.148	529.645	−6.744	248.891	94.9
H-7	449.91	3.531	−5.014	404.583	−5.855	465.211	94.3
H-8	354.34	4.303	−5.741	449.975	−6.848	369.696	100.0
H-9	439.47	3.211	−5.633	170.607	−6.353	115.97	85.7
H-10	379.42	4.543	−5.415	1815.099	−5.731	3934.464	100.0
H-11	366.44	3.856	−5.801	479.882	−6.734	351.606	100.0
H-12	311.36	2.819	−4.128	1190.312	−5.96	1016.341	100.0
H-13	358.43	2.821	−5.446	212.297	−5.944	485.277	85.1
H-14	353.82	2.374	−4.248	423.574	−5.582	488.194	87.9
H-15	389.40	2.624	−4.935	315.658	−6.499	212.238	87.0
H-16	382.25	3.912	−5.302	722.184	−5.798	1907.87	100.0
H-17	364.35	2.784	−4.769	297.599	−5.636	436.066	87.5
H-18	399.91	2.938	−5.06	389.469	−5.933	612.545	90.5
H-19	360.37	3.361	−5.262	557.24	−7.478	262.937	95.8
H-20	432.51	3.182	−4.829	733.284	−6.303	579.626	96.9
H-21	448.36	4.032	−5.884	426.14	−6.403	644.099	100.0
H-22	466.96	3.253	−5.797	418.096	−6.316	775.967	92.9
H-23	309.37	3.645	−4.814	1199.414	−6.404	602.152	100.0
H-24	338.36	3.507	−5.252	834.936	−6.758	407.068	100.0

Recommended values are: [a]Molecular weight (<500); [b]QP log P for octanol/water (−2.0 to 6.5); [c]QPlog S: Predicted aqueous solubility, S in mol dm^{-3} (−6.5 to 0.5); [d]Apparent Caco-2 cell permeability (nm/s) (<25 poor, >500 great); [e]log HERG: HERG K^+ channel blockage (<−5); [f]Apparent MDCK permeability (nm/s) (<25 poor, >500 great); [g] % Human oral absorption (>80% is high &<25% is poor); *Zero number of violations from Lipinski's rule of five.

2.3.11 Density functional theory

The frontier molecular orbitals HOMO and LUMO of chemical species are very important indicators of their reactivity and also stability of the ligand-receptor

interactions [93]. The stability of interactions is inversely correlated to the energy gap between HOMO and LUMO orbitals. The orbital energy of all energetically stable hit molecules was calculated by using DFT. The high value of HOMO energy is likely to indicate the tendency of the molecule to donate electrons to an appropriate acceptor molecule with LUMO. The correlation of HOMO energies with IC_{50} data indicated that the HOMO of the inhibitor might transfer its electrons to less energy LUMO, of some amino residues in the active site of MMP-9. The calculated DFT properties of all hits with the most active (compound **48**) and least active (compound **36**) inhibitors are presented in **Table 2.13**. The HOMO-LUMO energy gaps of all hits were minimal and in between −0.119 to −0.210 eV. ESP expresses the electron density distribution around the nuclei of the hits. The mean ESP of all the hits were compared to most active and least active known MMP-9 inhibitors from training set. The molecular electrostatic potential of most active and least active inhibitors from training set and hits (H-7) is pictured in **Figure 2.9**. The negative surface (red) represents the electron-rich regions, whereas, the positive surface (blue) signifies the electron deficient regions (**Figure 2.9**). The ESP data indicated that most of the compounds possessed both low and high electron density sites. The high and low electron density regions may correspond to the hydrogen bonding between the hits and MMP-9. An excellent agreement with DFT study results and docking study was observed for all the molecules.

2.3.12 Determination of MMP-9 selectivity

The final hits for MMP-9 selectivity were obtained by Glide XP docking studies with the crystal structure of MMP-2, and MMP-3. The corresponding docking scores for MMPs are listed in **Table 2.14**. Finally, nine hits *viz.* H-7, H-9, H-10, H-11, H-15, H-16, H-20, H-21 and H-22 (**Figure 2.10**) showed selective MMP-9 binding affinity over other MMPs (MMP-2 & MMP-3).

Table 2.13 Calculated DFT properties of most active, least active and hits

Hit	Solvation Energy (kcal/mol)	HOMO	LUMO	HOMO-LUMO gap	ESP means (kcal/mol)
H-1	−36.78	−0.225	−0.059	−0.166	−0.27
H-2	−25.16	−0.224	−0.040	−0.185	2.07
H-3	−23.64	−0.218	−0.038	−0.180	−1.04
H-4	−18.8	−0.228	−0.046	−0.182	0.89
H-5	−19.92	−0.225	−0.047	−0.178	1.05
H-6	−21.6	−0.215	−0.096	−0.119	0.68
H-7	−26.17	−0.214	−0.082	−0.132	−1.57
H-8	−21.27	−0.218	−0.053	−0.165	−0.06
H-9	−27.18	−0.221	−0.091	−0.130	0.44
H-10	−29.06	−0.227	−0.058	−0.168	1.57
H-11	−21.84	−0.185	−0.060	−0.124	1.29
H-12	−10.42	−0.216	−0.048	−0.168	−1.19
H-13	−17.92	−0.207	−0.054	−0.153	−1.54
H-14	−22.46	−0.230	−0.066	−0.164	−4.28
H-15	−21.11	−0.193	−0.037	−0.156	−2.36
H-16	−33.54	−0.234	−0.065	−0.169	2.24
H-17	−22.34	−0.220	−0.060	−0.160	−0.11
H-18	−31.8	−0.229	−0.053	−0.176	0.82
H-19	−22.61	−0.221	−0.068	−0.154	1.98
H-20	−20.07	−0.225	−0.063	−0.161	−0.95
H-21	−19.46	−0.240	−0.040	−0.200	3.62
H-22	−26.63	−0.219	−0.048	−0.171	−2.44
H-23	−19.99	−0.181	−0.071	−0.110	−0.01
H-24	−19.38	−0.223	−0.086	−0.137	−0.17
Least active	−22.37	−0.243	−0.033	−0.210	−2.07
Most active	−28.79	−0.240	−0.050	−0.190	4.59

The MMP-9 selectivity was shown by the compounds, which formed a smaller number of hydrogen bond(s) and the higher number of π–π and π–cationic bonds with the active site of MMP-9 (**Table 2.10**). The structural difference of selective MMP-9 hits and cocrystal ligand of 4XCT, N73 are depicted in **Figure 2.10**. The N73 had two hydrophobic isopropyl moieties, which were solvated in the binding pocket and reduced the binding interaction with MMP-9 (**Figure 2.11**). On the other hand, all the hits were

devoid of aliphatic moiety and showed better MMP-9 interactions. Selective MMP-9 hits possessed more aromatic moieties and no aliphatic/alicyclic group(s), which were favorable for π-π and π-cationic interactions.

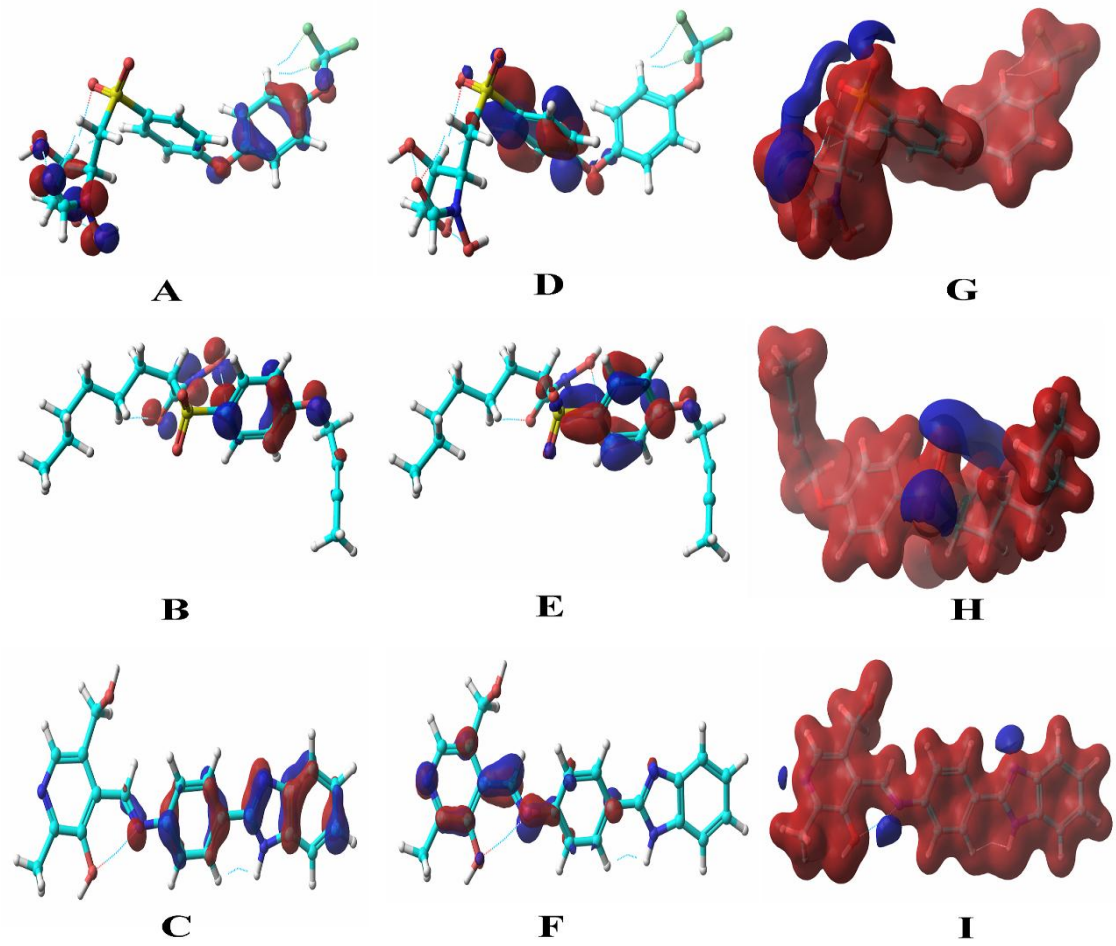

Figure 2.9 The HOMO map of most active inhibitor, A; least active inhibitor, B; and hit (H-7), C; the LUMO of most active, D; least active, E; and H-7, F; and molecular electrostatic potential (MESP) picture of most active, G; least active, H; and H-7, I.

2.3.13 *In vitro* MMP-9 enzyme inhibition

Four hits, *i.e.*, ZINC06455433, ZINC21212924, ZINC09613137, and ZINC23114578 (H-2, H-5, H-9, and H-13 respectively) were selected based on better docking score, MMP-9 selectivity, and ADME properties (**Figure 2.11**). *In vitro*, MMP-9 inhibition assay was performed with reference NNGH. Among hits, ZINC23114578 (IC_{50}

81.22±0.231 nM) produced better MMP-9 inhibition than other three (ZINC06455433, ZINC21212924, and ZINC09613137; IC_{50} values 277.61±0.122, 122.98±0.153, and 242.92±0.119 nM respectively) (**Table 2.15**). The potency of hits in inhibiting MMP-9 (IC_{50}) was calculated by constructing a dose-response curve (**Figure 2.12**) utilizing GraphPad Prism 5.0.

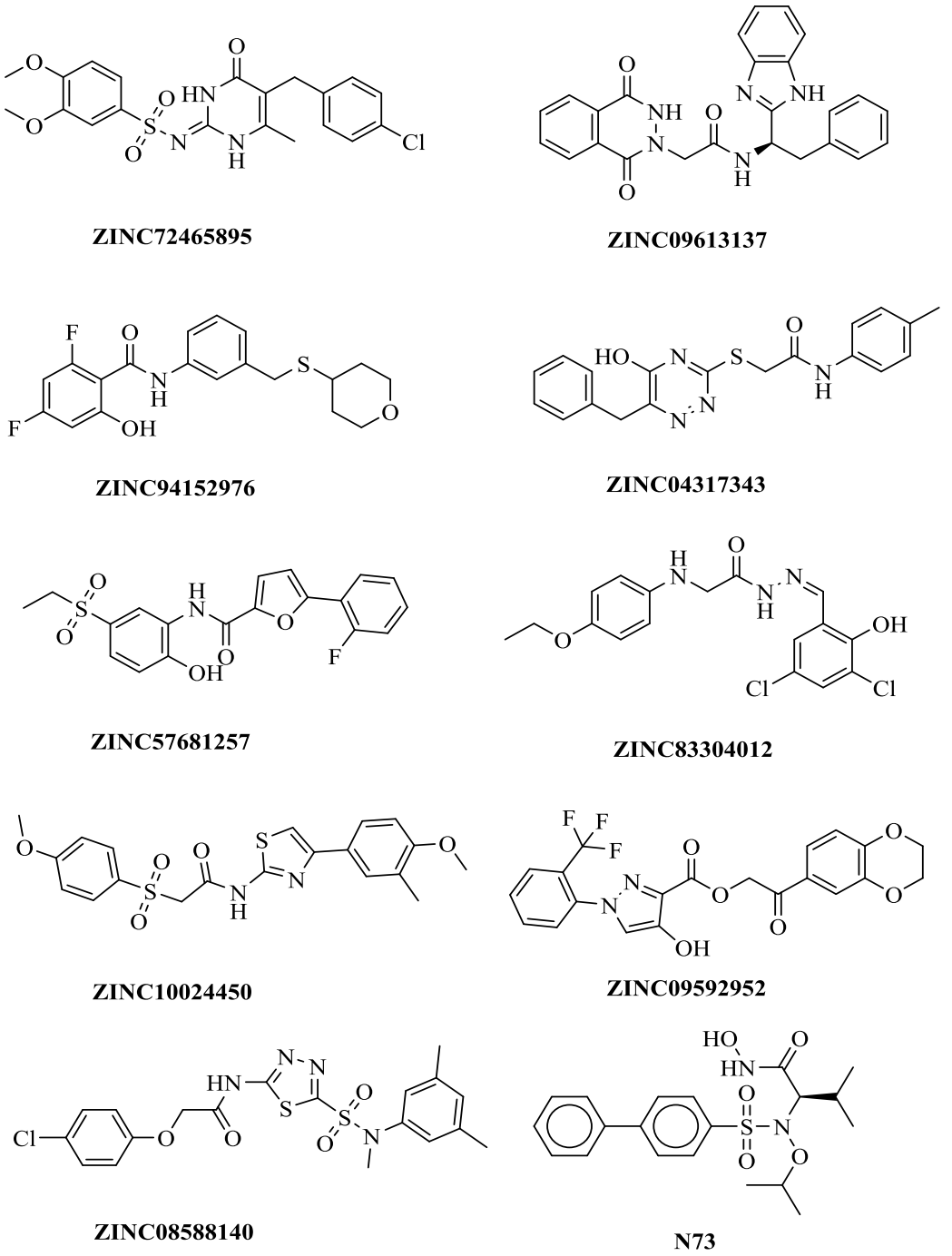

Figure 2.10 Structure of N73 and final hits with selective MMP-9 binding affinity.

Table 2.14 Glide docking scores of hits with MMP-2, MMP-3 and MMP-9 with cocrystal ligand of respective crystal structures

Compound	MMP-9	MMP-2	MMP-3	Selectivity
H-1	−11.737	−11.602	−11.679	Non-selective
H-2	−11.122	−11.301	−12.542	Non-selective
H-3	−11.058	−9.908	−10.851	Non-selective
H-4	−11.053	−10.307	−7.88	Non-selective
H-5	−10.371	−11.553	−11.652	Non-selective
H-6	−10.327	−10.936	−11.04	Non-selective
H-7	−10.322	*	*	MMP-9
H-8	−10.106	−11.195	−11.036	Non-selective
H-9	−10.03	*	*	MMP-9
H-10	−9.983	*	*	MMP-9
H-11	−9.783	*	*	MMP-9
H-12	−9.705	−6.603	−11.481	Non-selective
H-13	−9.67	−11.402	−11.642	Non-selective
H-14	−9.524	−9.111	−10.823	Non-selective
H-15	−9.434	*	*	MMP-9
H-16	−9.406	*	*	MMP-9
H-17	−9.392	−9.63	−8.897	Non-selective
H-18	−9.377	−9.927	−10.657	Non-selective
H-19	−9.375	−10.499	−10.85	Non-selective
H-20	−9.251	*	*	MMP-9
H-21	−9.06	*	*	MMP-9
H-22	−9.029	*	*	MMP-9
H-23	−9.024	−11.164	−10.819	Non-selective
H-24	−9.019	−11.926	−11.889	Non-selective
Cocrystal ligand	−8.355	−8.204	−9.964	Non-selective

*No docking score or very high docking score with respective protein structure.

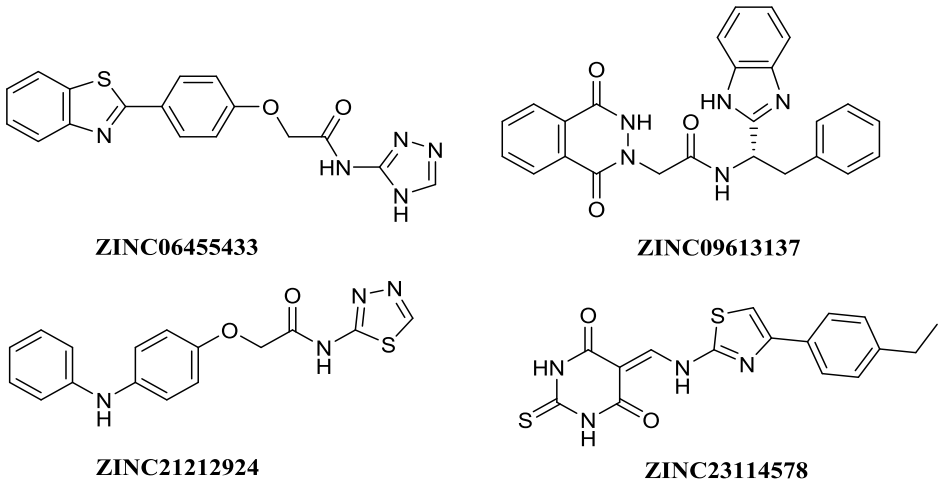

Figure 2.11 Selected hits for *in vitro* studies

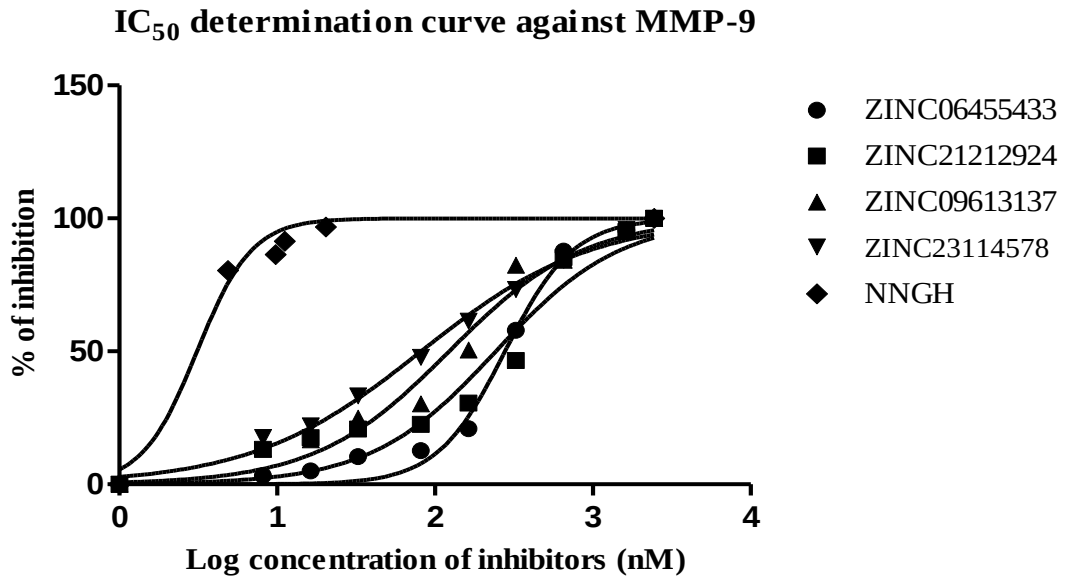

Figure 2.12 Dose-response curves of hits with reference NNGH against MMP-9.

Table 2.15 Inhibitory activity of hits on human MMP-9, AChE, BuChE and propidium displacement asssay

Compound	IC_{50}(nM) MMP-9[a]	IC_{50}(nM) AChE[a]	IC_{50}(nM) BuChE[a]	Propidium displacement (%)		
				0.24 µM	1 µM	3 µM
ZINC06455433	277.61±0.12	441.9±0.11	65272±0.16	68	75	100
ZINC21212924	122.98±0.15	800.2±0.26	45636±0.23	42	56	76
ZINC09613137	242.92±0.12	625.4±0.10	64870±0.12	12	30	76
ZINC23114578	81.22±0.23	643.2±0.058	65026±0.24	55	80	100
NNGH	1.07±0.06	-	-	-	-	-
Donepezil	-	23.44±0.53	7414±3.7	0	0	0

[a]Each assay was repeated three independent times and data are expressed as mean ± SEM.

2.3.14 *In vitro* blood-brain barrier permeation assay

A parallel artificial membrane permeation assay of the blood-brain barrier (PAMPA-BBB) was performed as the method described by to explore whether the selected hits can infiltrate into the brain Di *et al*. [97]. The *in vitro* permeability (Pe) of the four hits (**Table 2.16**) and nine commercially available drugs (**Table 2.17**) was determined through a lipid extract of porcine brain lipid in PBS. The assay was validated by comparing the experimentally obtained permeability [Pe(exp)] of nine drugs with the reported values of permeation [Pe(literature)] offering a linear relationship, *i.e.*,

Pe (exp) = 1.308 Pe (literature) − 0.8394, (R^2 = 0.9317).

The compounds with permeability values (Pe) greater than 4.3 × 10^{-6} cm.s^{-1} were highly capable of CNS permeability and Pe value less than 1.8 × 10^{-6} cm.s^{-1} was poorly permeability of CNS (**Figure 2.13** & **Table 2.16**). The tested compounds demonstrated permeability values above 4.3 × 10^{-6} cm.s^{-1} and were a pointer toward their potential to comfortably cross the BBB by passive diffusion.

Table 2.16 Permeability determined by BBB-PAMPA study of hits

Compound	Pe [10^{-6} cm s^{-1}][a*]	Prediction[b]
ZINC06455433	4.440±0.041	CNS+
ZINC09613137	8.167±0.039	CNS+
ZINC21212924	5.901±0.036	CNS+
ZINC23114578	8.055±0.039	CNS+

[a]Data expressed as mean ± SEM of three independent experiments. [b]CNS+ indicates good passive CNS permeation; *Permeability (Pe 10^{-6}) express in cm.s^{-1}.

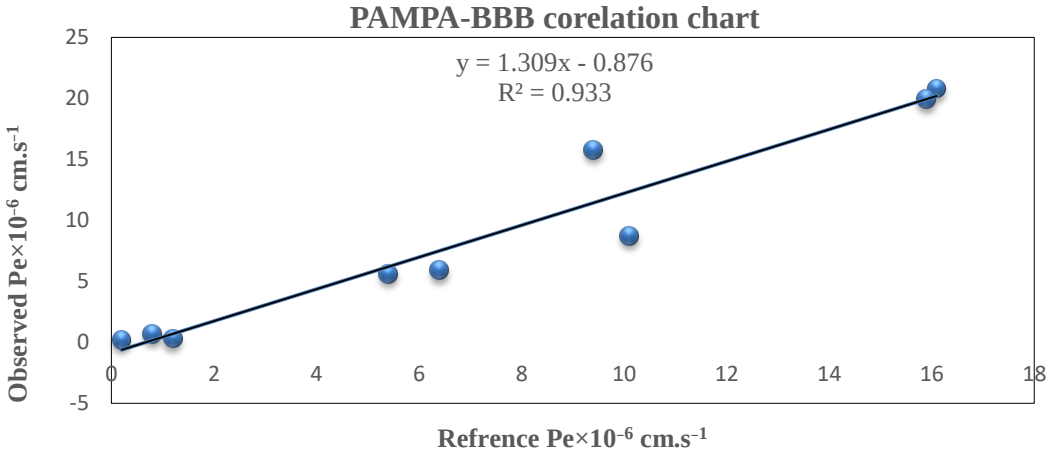

Figure 2.13 Linear correlations between experimental and reported permeability of commercial drugs for PAMPA-BBB assay.

2.3.15 Cytotoxicity and neuroprotection assessment

The cell viability and neuroprotective potential, against apoptosis of selected hits, were assessed on human neuroblastoma SH-SY5Y cell line. To investigate the cytotoxicity of compounds, cells were exposed to considerably high concentrations of the test compounds (50 μM and 100 μM) for 24 h, which was followed by determination of the cell viability utilizing 3-(4,5-dimethylthiazol- 2-yl)-2,5-diphenyltetrazolium bromide

(MTT) assay. The selected compounds showed negligible cell death even at high concentrations (**Table 2.18**). The neuroprotective potential of the selected hit molecules was assessed using L-glutamate as excitotoxicity. In this assay, the addition of L-glutamate (100 μM) to the growth media caused significant cell death, as was evidenced by the reduction in cell viability. The results (**Table 2.18**) are the mean ± SEM of at least three independent experiments.

Table 2.17 Permeability of nine commercial drugs for PAMPA-BBB assay used to validate the experiment

Commercial drug	**Reference value Pe (10^{-6})[a*]**	**Experimental value Pe (10^{-6})[b*]**
Verapamil	16	20.81±1.2
Diazepam	16	19.9±0.5
Progesterone	9.3	15.79±1.4
Atenolol	0.8	0.68±0.4
Dopamine	0.2	0.17±0.1
Lomefloxacin	1.1	0.31±0.3
Alprazolam	5.4	4.6±0.7
Chlorpromazine	6.5	5.9±0.6
Oxazepam	10	8.7±1.1

[a]Taken from literature. [b]Data are expressed as mean ± SEM of three independent experiments, *Permeability (Pe 10^{-6}) express in $cm.s^{-1}$.

Table 2.18 Cell viability and neuroprotection of hits on human neuroblastoma SH-SY5Y cell Line

Compound	**Cell viability (%)[a]**		**Neuroprotection (%)[b]**
	50 μM	**100 μM**	**25 μM**
ZINC06455433	88.24±0.617	75.76±0.089	10.38±0.080
ZINC09613137	77.10±0.295	76.57±0.335	26.52±0.060
ZINC21212924	87.02±0.047	78.76±0.189	12.23±0.062
ZINC23114578	82.87±0.317	81.82±0.221	5.48±0.047

[a]Percentage cell viability of SH-SY5Y cells exposed at relatively high concentrations (50 μM and 100 μM) of test compounds. [b]Percentage neuroprotection of SH-SY5Y cells at relatively lower concentrations (25 μM) of the test compounds against L-glutamate (100 μM).

2.3.16 Molecular dynamics simulation

The analyses of molecular dynamic (MD) simulation of N73 and ZINC21212924 with 4XCT were undertaken to establish the binding potency and interactions of amino acid residues. In MD simulations, RMSD of the protein backbone C-α atoms and individual inhibitor, root mean square fluctuation (RMSF) in the individual amino acid side chain and ligand-protein interactions were recorded concerning time throughout 50 ns of simulation. The total energy of dynamic ligand-protein complexes was found stable in last 40ns of the entire simulation. Furthermore, temperature, pressure, volume, and potential energy of the complex remained constant, indicating the robustness and reliability of MD simulations. The RMSD of simulation converging between 0.5 and 3.0Å, denoted the stability of macromolecular ligand-protein complexes during 50ns simulation. The RMSF in individual amino acid residues during the entire simulation was below 4.0Å for N73 and 3.0Å for ZINC21212924, indicating a lower degree of conformational changes in the side chains.

After the initial 10ns simulation, RMSD of protein backbone C-α along with the ligand RMSD values were stabilized. RMSD plot of RMSD values for protein were displayed on the left Y-axis, for ligand these values on the right Y-axis (**Figure 2.14)**; protein backbone in green, and ligand in maroon. The mean RMSD value for the N73-4XCT complex was 1.8Å, whereas, for ZINC21212924-4XCT complex, it was 1.7Å. RMSF was useful for characterizing local changes along the protein chain C-α and peaks indicated areas of the protein that fluctuate the most during the simulation. RMSF values of hit ZINC21212924 below 3.0Å and N73 below 4.0Å, indicated less fluctuation and better stability of hit-protein complex during simulation (**Figure 2.15**). The interaction of N73 and ZINC21212924 with MMP-9 was higher than 30% after MD simulation (**Figure 2.16)**. MD study revealed that ZINC21212924 interacted

Ala191 and Glu227 with H-bonding and N73 interacted Leu188 and Glu227 with H-bond formation and His226 and Try248 with π-π stacking; the study also demonstrated that all the ligands were interacting with protein at Glu227 and Zn302 at the active site of MMP-9.

2.4 Conclusions

The available X-ray crystal structures of MMP-9 bound to cocrystal inhibitors in the active site, combined with ligands having known inhibitory activity, were utilized for pharmacophore-based screening. It was followed by high-throughput virtual screening and molecular docking to obtain potent hits. The e-pharmacophore hypotheses and 3D-QSAR predictions retrieved total of 24 hits with diverse scaffolds, good ADME properties and without ZBG as MMPs inhibitor.

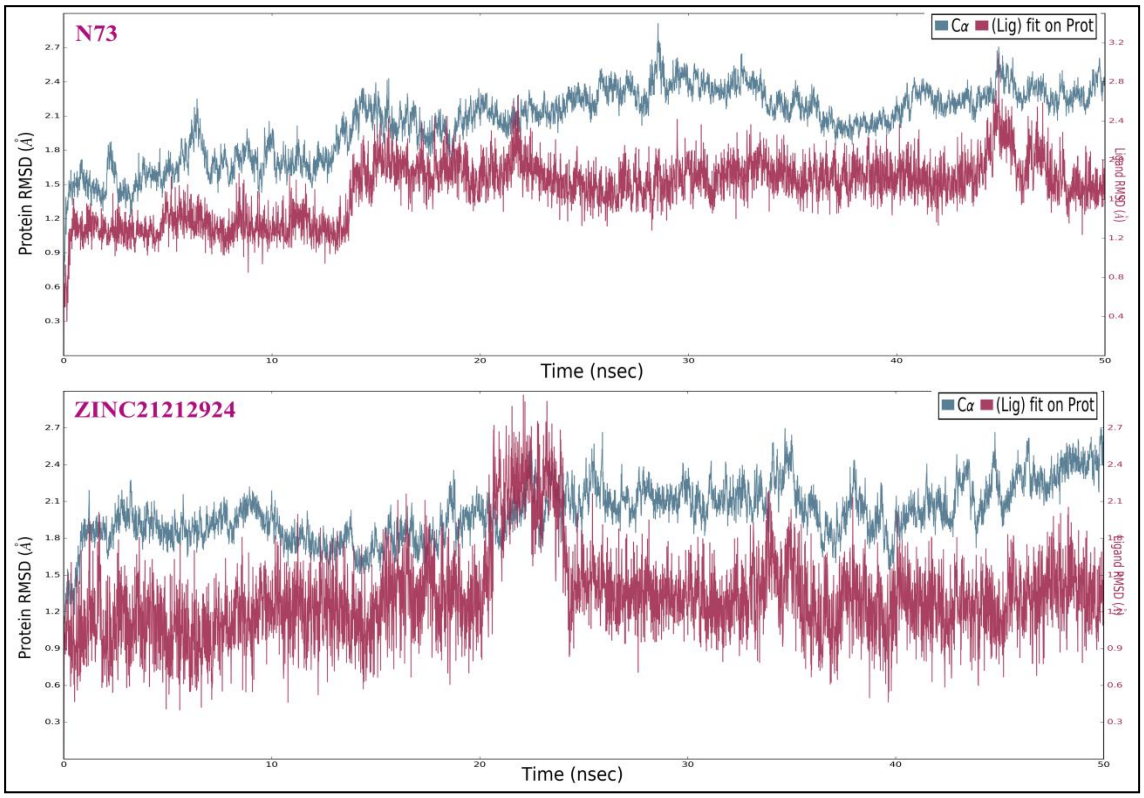

Figure 2.14 RMSD plot of RMSD values (N73-4XCT and ZINC21212924-4XCT complexes) for protein on the left Y-axis and for ligand on the right Y-axis; protein backbone in green, and ligand in maroon.

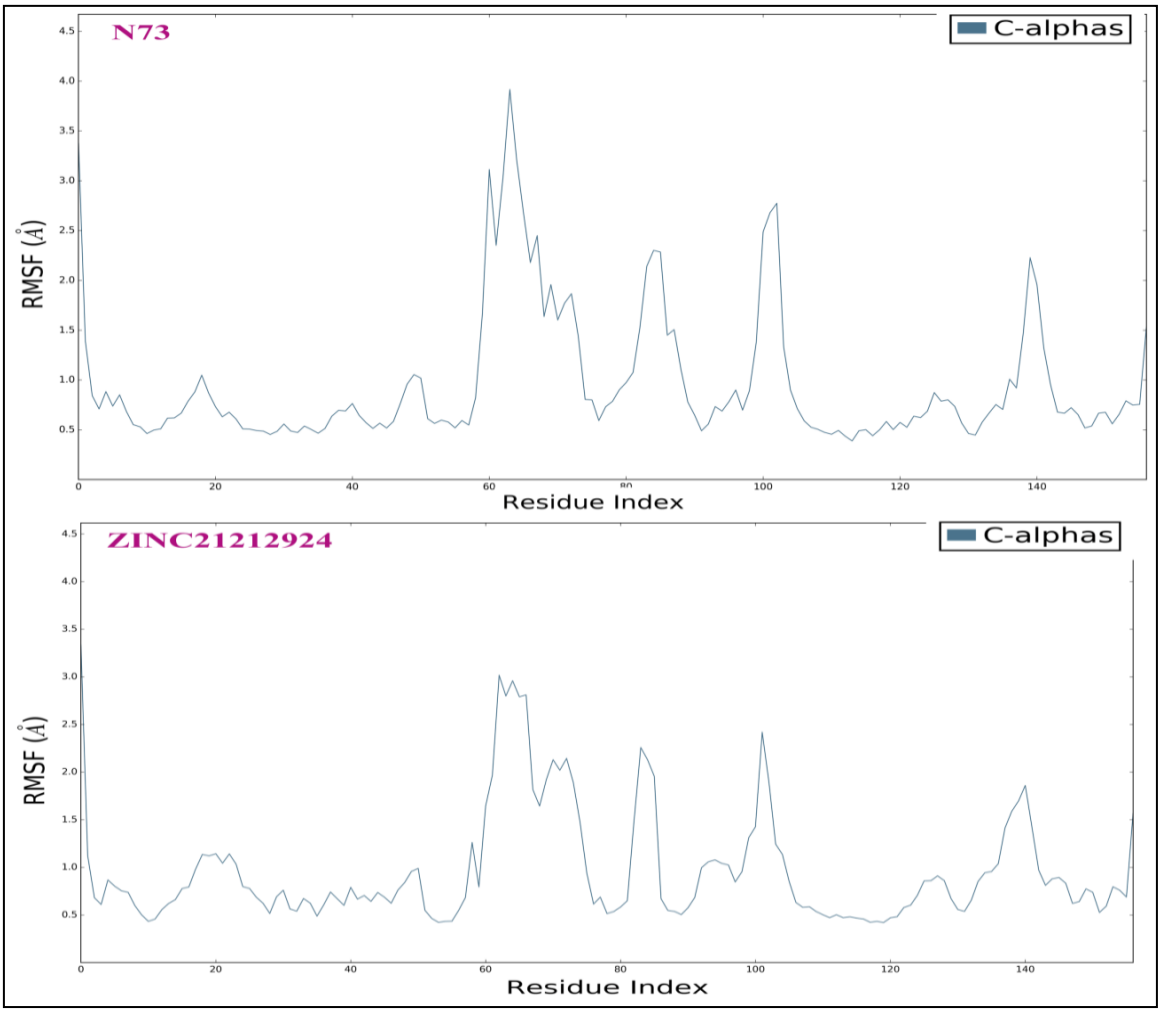

Figure 2.15 RMSF of the protein C-α chain in N73-4XCT and ZINC21212924-4XCT complexes.

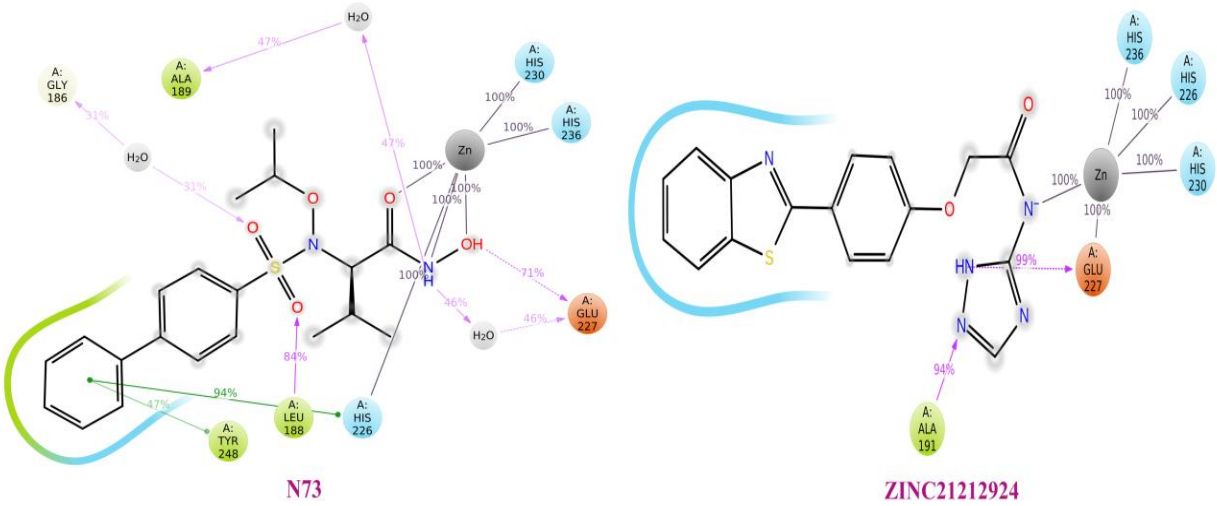

Figure 2.16 Schematic diagrams of detailed ligand (N73 and ZINC21212924) interactions with amino acid residues of MMP-9 after MD simulation.

Out of these hits, nine had better MMP-9 binding affinity than to other MMPs, and these compounds were expected to produce selective MMP-9 inhibition. The cocrystal of 4XCT, N73 interacted with Leu188, Ala189, and Glu227 by hydrogen-bonding interaction, His226, π–π stacking interaction, and Zn302, a salt-bridge. Whereas, H-7 (hit with MMP-9 selectivity) interacted with Ala191, Glu227 by hydrogen-bonding, His226, π–π stacking and Zn302, a salt-bridge. The IFD, DFT, and AutoDock studies also supported the binding affinity and interaction of the hits. MMP-9 selectivity was determined from Glide docking scores and compounds H-7, H-9, H-10, H-11, H-15, H-16, H-20, H-21, and H-22 were found to be selective MMP-9 inhibitors with less adverse effects. Finally, the docking study of hits by AutoDock also showed that hits were more potent than existing MMP-9 inhibitors. *In vitro* MMP-9 enzyme assays of four hits *viz.* H-2, H-5, H-9, and H-13 (ZINC06455433, ZINC09613137, ZINC21212924, and ZINC23114578) supported the *in-silico* results. The hits had attractive IC_{50} values, *i.e.*, 81.22±0.231, 277.61±0.122, 122.98±0.153, and 242.92±0.119 nM (ZINC23114578, ZINC06455433, ZINC21212924, and ZINC09613137 respectively), with insignificant toxicity against neuroblastoma SH-SY5Y cell, good BBB permeability, and neuroprotectivity against L-glutamate induced excitotoxicity.

2.5 References

[1] T. Wei, H. Zhang, N. Cetin, E. Miller, T. Moak, J.Y. Suen, G.T. Richter, Elevated Expression of Matrix Metalloproteinase-9, not Matrix Metalloproteinase-2 Contributes to Progression of Extracranial Arteriovenous Malformation, *Scientific Reports*, 6 (2016). 24378.

[2] T. Itoh, H. Matsuda, M. Tanioka, K. Kuwabara, S. Itohara, R. Suzuki, The role of matrix metalloproteinase-2 and matrix metalloproteinase-9 in antibody-induced arthritis, *The Journal of Immunology*, 169 (2002) 2643–2647.

[3] H.P. Hartung, B.C. Kieseier, The role of matrix metalloproteinases in autoimmune damage to the central and peripheral nervous system, *Journal of Neuroimmunology*, 107 (2000) 140–147.

[4] J. Uhm, N. Dooley, J.G. Villemure, V. Yong, Mechanisms of glioma invasion: role of matrix-metalloproteinases, *Canadian Journal of Neurological Sciences*, 24 (1997) 3–15.

[5] S. Jung, K. S. Moon, S. T. Kim, H. H. Ryu, Y. H. Lee, Y. I. Jeong, T. Y. Jung, I. Y. Kim, K. K. Kim, S. S. Kang, Increased expression of intracystic matrix metalloproteinases in brain tumors: relationship to the pathogenesis of brain tumor-associated cysts and peritumoral edema, *Journal of Clinical Neuroscience*, 14 (2007) 1192–1198.

[6] A.M. Planas, S. Solé, C. Justicia, Expression and activation of matrix metalloproteinase-2 and-9 in rat brain after transient focal cerebral ischemia, *Neurobiology of Disease*, 8 (2001) 834–846.

[7] J. Castillo, eacute, I. Rodríguez, Biochemical changes and inflammatory response as markers for brain ischaemia: molecular markers of diagnostic utility and prognosis in human clinical practice, *Cerebrovascular Diseases*, 17 (2003) 7–18.

[8] J. Kurzepa, A. Szczepanska-Szerej, M. Stryjecka-Zimmer, T. Malecka-Massalska, Z. Stelmasiak, Simvastatin could prevent increase of the serum MMP-9/TIMP-1 ratio in acute ischaemic stroke, *Folia Biologica*, 52 (2006) 181–183.

[9] Y. Shigemori, Y. Katayama, T. Mori, T. Maeda, T. Kawamata, Matrix metalloproteinase-9 is associated with blood-brain barrier opening and brain edema formation after cortical contusion in rats, in Brain Edema XIII, *Acta Neurochirurgica, Springer-Verlag*, 96 (2006) 130–133.

[10] M. Petty, J. Wettstein, Elements of cerebral microvascular ischaemia, *Brain Research Reviews*, 36 (2001) 23–34.

[11] S. Chandler, R. Coates, A. Gearing, J. Lury, G. Wells, E. Bone, Matrix metalloproteinases degrade myelin basic protein, *Neuroscience Letters*, 201 (1995) 223–226.

[12] G.E. Terp, G. Cruciani, I.T. Christensen, F.S. Jørgensen, Structural differences of matrix metalloproteinases with potential implications for inhibitor selectivity examined by the GRID/CPCA approach, *Journal of Medicinal Chemistry*, 45 (2002) 2675–2684.

[13] E. Morgunova, A. Tuuttila, U. Bergmann, M. Isupov, Y. Lindqvist, G. Schneider, K. Tryggvason, Structure of human pro-matrix metalloproteinase-2: activation mechanism revealed, *Science*, 284 (1999) 1667–1670.

[14] R.E. Vandenbroucke, C. Libert, Is there new hope for therapeutic matrix metalloproteinase inhibition?, Nature reviews Drug discovery, 13 (2014) 904-927.

[15] S. Kalva, K. Saranyah, P.R. Suganya, M. Nisha, L.M. Saleena, Potent inhibitors precise to S1′ loop of MMP-13, a crucial target for osteoarthritis, *Journal of Molecular Graphics and Modelling*, 44 (2013) 297–310.

[16] D. Pradiba, M. Aarthy, V. Shunmugapriya, S.K. Singh, M. Vasanthi, Structural insights into the binding mode of flavonols with the active site of Matrix MetalloProteinase-9 through molecular docking and Molecular Dynamic Simulations studies, *Journal of Biomolecular Structure and Dynamics*, (2017) 1–22.

[17] H. Othman, S.A. Wieninger, M. ElAyeb, M. Nilges, N. Srairi-Abid, *In silico* prediction of the molecular basis of ClTx and AaCTx interaction with matrix metalloproteinase-2 (MMP-2) to inhibit glioma cell invasion, *Journal of Biomolecular Structure and Dynamics*, 35 (2017) 2815–2829.

[18] Y. Wang, L. Yang, J. Hou, Q. Zou, Q. Gao, W. Yao, Q. Yao, J. Zhang, Hierarchical Virtual Screening of the Dual MMP-2/HDAC-6 Inhibitors from Natural Products Based on Pharmacophore Models and Molecular Docking, *Journal of Biomolecular Structure and Dynamics*, (2018) 1–59.

[19] A. Nash, H.L. Birch, N.H. de Leeuw, Mapping intermolecular interactions and active site conformations: from human MMP-1 crystal structure to molecular dynamics free energy calculations, *Journal of Biomolecular Structure and Dynamics*, 35 (2017) 564–573.

[20] S. Kalva, E.A. Singam, V. Rajapandian, L.M. Saleena, V. Subramanian, Discovery of potent inhibitor for matrix metalloproteinase-9 by pharmacophore based modeling and dynamics simulation studies, *Journal of Molecular Graphics and Modelling*, 49 (2014) 25–37.

[21] K. Loving, N.K. Salam, W. Sherman, Energetic analysis of fragment docking and application to structure-based pharmacophore hypothesis generation, *Journal of Computer-Aided Molecular Design*, 23 (2009) 541–554.

[22] H.M. Berman, J. Westbrook, Z. Feng, G. Gilliland, T.N. Bhat, H. Weissig, I.N. Shindyalov, P.E. Bourne, The protein data bank, *Nucleic Acids Research*, 28 (2000) 235–242.

[23] E. Nuti, A.R. Cantelmo, C. Gallo, A. Bruno, B. Bassani, C. Camodeca, T. Tuccinardi, L. Vera, E. Orlandini, S. Nencetti, N-O-Isopropyl Sulfonamido-Based Hydroxamates as Matrix Metalloproteinase Inhibitors: Hit Selection and *in vivo* Antiangiogenic Activity, *Journal of Medicinal Chemistry*, 58 (2015) 7224–7240.

[24] C. Antoni, L. Vera, L. Devel, M.P. Catalani, B. Czarny, E. Cassar-Lajeunesse, E. Nuti, A. Rossello, V. Dive, E.A. Stura, Crystallization of bi-functional ligand-protein complexes, *Journal of Structural Biology*, 182 (2013) 246–254.

[25] C. Camodeca, E. Nuti, L. Tepshi, S. Boero, T. Tuccinardi, E.A. Stura, A. Poggi, M.R. Zocchi, A. Rossello, Discovery of a new selective inhibitor of A Disintegrin And Metalloprotease 10 (ADAM-10) able to reduce the shedding of NKG2D ligands in Hodgkin's lymphoma cell models, *European Journal of Medicinal Chemistry*, 111 (2016) 193–201.

[26] A. Tochowicz, K. Maskos, R. Huber, R. Oltenfreiter, V. Dive, A. Yiotakis, M. Zanda, W. Bode, P. Goettig, Crystal structures of MMP-9 complexes with five inhibitors: contribution of the flexible Arg424 side-chain to selectivity, *Journal of Molecular Biology*, 371 (2007) 989–1006.

[27] S. Rowsell, P. Hawtin, C.A. Minshull, H. Jepson, S.M. Brockbank, D.G. Barratt, A.M. Slater, W.L. McPheat, D. Waterson, A.M. Henney, Crystal structure of human MMP9 in complex with a reverse hydroxamate inhibitor, *Journal of Molecular Biology*, 319 (2002) 173–181.

[28] G.A. Kaminski, R.A. Friesner, J. Tirado-Rives, W.L. Jorgensen, Evaluation and reparametrization of the OPLS-AA force field for proteins via comparison with accurate quantum chemical calculations on peptides, *The Journal of Physical Chemistry B*, 105 (2001) 6474–6487.

[29] T.A. Halgren, R.B. Murphy, R.A. Friesner, H.S. Beard, L.L. Frye, W.T. Pollard, J.L. Banks, Glide: a new approach for rapid, accurate docking and scoring. 2. Enrichment factors in database screening, *Journal of Medicinal Chemistry*, 47 (2004) 1750–1759.

[30] J.F. Truchon, C.I. Bayly, Evaluating virtual screening methods: good and bad metrics for the “early recognition” problem, *Journal of Chemical Information and Modeling*, 47 (2007) 488–508.

[31] B. Fabre, A. Ramos, B. de Pascual-Teresa, Targeting matrix metalloproteinases: Exploring the dynamics of the S1′ pocket in the design of selective, small molecule inhibitors: Miniperspective, *Journal of Medicinal Chemistry*, 57 (2014) 10205–10219.

[32] Y.M. Zhang, X. Fan, D. Chakaravarty, B. Xiang, R.H. Scannevin, Z. Huang, J. Ma, S.L. Burke, P. Karnachi, K.J. Rhodes, 1-Hydroxy-2-pyridinone-based MMP inhibitors: synthesis and biological evaluation for the treatment of ischemic stroke, *Bioorganic & Medicinal Chemistry Letters*, 18 (2008) 409–413.

[33] L.J. Wilson, B. Wang, S.-M. Yang, R.H. Scannevin, S.L. Burke, P. Karnachi, K.J. Rhodes, W.V. Murray, Discovery of novel Cobactin-T based matrix metalloproteinase inhibitors via a ring closing metathesis strategy, *Bioorganic & Medicinal Chemistry Letters*, 21 (2011) 6485–6490.

[34] E. Nuti, E. Orlandini, S. Nencetti, A. Rossello, A. Innocenti, A. Scozzafava, C.T. Supuran, Carbonic anhydrase and matrix metalloproteinase inhibitors. Inhibition of human tumor-associated isozymes IX and cytosolic isozyme I and II with sulfonylated hydroxamates, *Bioorganic & Medicinal Chemistry*, 15 (2007) 2298–2311.

[35] A.M. Venkatesan, J.M. Davis, G.T. Grosu, J. Baker, A. Zask, J.I. Levin, J. Ellingboe, J.S. Skotnicki, J.F. DiJoseph, A. Sung, Synthesis and Structure-Activity Relationships of 4-alkynyloxy Phenyl Sulfanyl, Sulfinyl, and Sulfonyl Alkyl

Hydroxamates as Tumor Necrosis Factor-α Converting Enzyme and Matrix Metalloproteinase Inhibitors, *Journal of Medicinal Chemistry*, 47 (2004) 6255–6269.

[36] K. Park, A. Aplasca, M.T. Du, L. Sun, Y. Zhu, Y. Zhang, J.I. Levin, Design and synthesis of butynyloxyphenyl β-sulfone piperidine hydroxamates as TACE inhibitors, *Bioorganic & Medicinal Chemistry Letters*, 16 (2006) 3927–3931.

[37] O. Nicolotti, M. Catto, I. Giangreco, M. Barletta, F. Leonetti, A. Stefanachi, L. Pisani, S. Cellamare, P. Tortorella, F. Loiodice, Design, synthesis and biological evaluation of 5-hydroxy, 5-substituted-pyrimidine-2, 4, 6-triones as potent inhibitors of gelatinases MMP-2 and MMP-9, *European Journal of Medicinal Chemistry*, 58 (2012) 368–376.

[38] V. Aranapakam, J.M. Davis, G.T. Grosu, J. Baker, J. Ellingboe, A. Zask, J.I. Levin, V.P. Sandanayaka, M. Du, J.S. Skotnicki, Synthesis and structure-activity relationship of N-substituted 4-arylsulfonylpiperidine-4-hydroxamic acids as novel, orally active matrix metalloproteinase inhibitors for the treatment of osteoarthritis, *Journal of Medicinal Chemistry*, 46 (2003) 2376–2396.

[39] V. Aranapakam, G.T. Grosu, J.M. Davis, B. Hu, J. Ellingboe, J.L. Baker, J.S. Skotnicki, A. Zask, J.F. DiJoseph, A. Sung, Synthesis and structure-activity relationship of α-sulfonyl hydroxamic acids as novel, orally active matrix metalloproteinase inhibitors for the treatment of osteoarthritis, *Journal of Medicinal Chemistry*, 46 (2003) 2361–2375.

[40] R.P. Verma, C. Hansch, Matrix metalloproteinases (MMPs): chemical–biological functions and (Q) SARs, Bioorganic & medicinal chemistry, 15 (2007) 2223-2268.

[41] R. Kiyama, Y. Tamura, F. Watanabe, H. Tsuzuki, M. Ohtani, M. Yodo, Homology modeling of gelatinase catalytic domains and docking simulations of novel sulfonamide inhibitors, *Journal of Medicinal Chemistry*, 42 (1999) 1723–1738.

[42] Y. Tamura, F. Watanabe, T. Nakatani, K. Yasui, M. Fuji, T. Komurasaki, H. Tsuzuki, R. Maekawa, T. Yoshioka, K. Kawada, Highly selective and orally active inhibitors of type IV collagenase (MMP-9 and MMP-2): N-sulfonylamino acid derivatives, *Journal of Medicinal Chemistry*, 41 (1998) 640–649.

[43] Y.M. Zhang, X. Fan, B. Xiang, D. Chakravarty, R. Scannevin, S. Burke, P. Karnachi, K. Rhodes, P. Jackson, Synthesis and SAR of α-sulfonylcarboxylic acids as potent matrix metalloproteinase inhibitors, *Bioorganic & Medicinal Chemistry Letters*, 16 (2006) 3096–3100.

[44] D.P. Becker, T.E. Barta, L.J. Bedell, T.L. Boehm, B.R. Bond, J. Carroll, C.P. Carron, G.A. DeCrescenzo, A.M. Easton, J.N. Freskos, Orally active MMP-1 sparing α-tetrahydropyranyl and α-piperidinyl sulfone matrix metalloproteinase (MMP) inhibitors with efficacy in cancer, arthritis, and cardiovascular disease, *Journal of Medicinal Chemistry*, 53 (2010) 6653–6680.

[45] H. Zhong, M.A. Wees, T.D. Faure, C. Carrillo, J. Arbiser, J.P. Bowen, The impact of ionization states of matrix metalloproteinase inhibitors on docking-based inhibitor design, *ACS Medicinal Chemistry Letters*, 2 (2011) 455–460.

[46] T. Le Diguarher, A.M. Chollet, M. Bertrand, P. Hennig, E. Raimbaud, M. Sabatini, N. Guilbaud, A. Pierré, G.C. Tucker, P. Casara, Stereospecific synthesis of 5-substituted 2-bisarylthiocyclopentane carboxylic acids as specific matrix metalloproteinase inhibitors, *Journal of Medicinal Chemistry*, 46 (2003) 3840–3852.

[47] A. Biasone, P. Tortorella, C. Campestre, M. Agamennone, S. Preziuso, M. Chiappini, E. Nuti, P. Carelli, A. Rossello, F. Mazza, α-Biphenylsulfonylamino 2-methylpropyl phosphonates: Enantioselective synthesis and selective inhibition of MMPs, *Bioorganic & Medicinal Chemistry*, 15 (2007) 791–799.

[48] S. Wagner, H.J. Breyholz, M.P. Law, A. Faust, C. Höltke, S. Schröer, G. Haufe, B. Levkau, O. Schober, M. Schäfers, Novel fluorinated derivatives of the broad-spectrum MMP inhibitors N-hydroxy-2 (R)-[[(4-methoxyphenyl) sulfonyl](benzyl) and (3-picolyl)-amino]-3-methyl-butanamide as potential tools for the molecular imaging of activated MMPs with PET, *Journal of Medicinal Chemistry*, 50 (2007) 5752–5764.

[49] S.M. Yang, R.H. Scannevin, B. Wang, S.L. Burke, Z. Huang, P. Karnachi, L.J. Wilson, K.J. Rhodes, B. Lagu, W.V. Murray, β-N-Biaryl ether sulfonamide hydroxamates as potent gelatinase inhibitors: Part 2. Optimization of α-amino substituents, *Bioorganic & Medicinal Chemistry Letters*, 18 (2008) 1140–1145.

[50] H. Nara, K. Sato, T. Naito, H. Mototani, H. Oki, Y. Yamamoto, H. Kuno, T. Santou, N. Kanzaki, J. Terauchi, Discovery of novel, highly potent, and selective quinazoline-2-carboxamide-based matrix metalloproteinase (MMP)-13 inhibitors without a zinc binding group using a structure-based design approach, *Journal of Medicinal Chemistry*, 57 (2014) 8886–8902.

[51] L.A. Reiter, R.P. Robinson, K.F. McClure, C.S. Jones, M.R. Reese, P.G. Mitchell, I.G. Otterness, M.L. Bliven, J. Liras, S.R. Cortina, Pyran-containing sulfonamide hydroxamic acids: potent MMP inhibitors that spare MMP-1, *Bioorganic & Medicinal Chemistry Letters*, 14 (2004) 3389–3395.

[52] S.M. Yang, R.H. Scannevin, B. Wang, S.L. Burke, L.J. Wilson, P. Karnachi, K.J. Rhodes, B. Lagu, W.V. Murray, β-N-Biaryl ether sulfonamide hydroxamates as potent gelatinase inhibitors: Part 1. Design, synthesis, and lead identification, *Bioorganic & Medicinal Chemistry Letters*, 18 (2008) 1135–1139.

[53] J. Wang, S. O'Sullivan, S. Harmon, R. Keaveny, M.W. Radomski, C. Medina, J.F. Gilmer, Design of barbiturate–nitrate hybrids that Inhibit MMP-9 activity and secretion, *Journal of Medicinal Chemistry*, 55 (2012) 2154–2162.

[54] M.C. Noe, S.L. Snow, L.A. Wolf-Gouveia, P.G. Mitchell, L. Lopresti-Morrow, L.M. Reeves, S.A. Yocum, J.L. Liras, M. Vaughn, 3-Hydroxy-4-arylsulfonyl tetrahydropyranyl-3-hydroxamic acids are novel inhibitors of MMP-13 and aggrecanase, *Bioorganic & Medicinal Chemistry Letters*, 14 (2004) 4727-4730.

[55] Y.M. Zhang, X. Fan, S.M. Yang, R.H. Scannevin, S.L. Burke, K.J. Rhodes, P.F. Jackson, Syntheses and *in vitro* evaluation of arylsulfone-based MMP inhibitors with heterocycle-derived zinc-binding groups (ZBGs), *Bioorganic & Medicinal Chemistry Letters*, 18 (2008) 405–408.

[56] M. Behrends, S. Wagner, K. Kopka, O. Schober, M. Schaefers, S. Kumbhar, M. Waller, G. Haufe, New matrix metalloproteinase inhibitors based on γ-fluorinated α-aminocarboxylic and α-aminohydroxamic acids, *Bioorganic & Medicinal Chemistry*, 23 (2015) 3809–3818.

[57] H.J. Breyholz, M. Schäfers, S. Wagner, C. Höltke, A. Faust, H. Rabeneck, B. Levkau, O. Schober, K. Kopka, C-5-disubstituted barbiturates as potential molecular probes for noninvasive matrix metalloproteinase imaging, *Journal of Medicinal Chemistry*, 48 (2005) 3400–3409.

[58] T. Masuda, Y. Nakayama, Development of a water-soluble matrix metalloproteinase inhibitor as an intra-arterial infusion drug for prevention of restenosis after angioplasty, *Journal of Medicinal Chemistry*, 46 (2003) 3497–3501.

[59] E. Nuti, L. Panelli, F. Casalini, S.I. Avramova, E. Orlandini, S. Santamaria, S. Nencetti, T. Tuccinardi, A. Martinelli, G. Cercignani, Design, synthesis, biological evaluation, and NMR studies of a new series of arylsulfones as selective and potent matrix metalloproteinase-12 inhibitors, *Journal of Medicinal Chemistry*, 52 (2009) 6347–6361.

[60] V. Hugenberg, H.-J.r. Breyholz, B. Riemann, S. Hermann, O. Schober, M. Schäfers, U. Gangadharmath, V. Mocharla, H. Kolb, J. Walsh, A new class of highly potent matrix metalloproteinase inhibitors based on triazole-substituted hydroxamates:(radio) synthesis and *in vitro* and first *in vivo* evaluation, *Journal of Medicinal Chemistry*, 55 (2012) 4714–4727.

[61] B. Delouvrié, K. Al-Kadhimi, J.C. Arnould, S.T. Barry, D.A. Cross, M. Didelot, P.R. Gavine, H. Germain, C.S. Harris, A.M. Hughes, Structure–activity relationship of a series of non peptidic RGD integrin antagonists targeting α 5 β 1: Part 1, *Bioorganic & Medicinal Chemistry Letters*, 22 (2012) 4111–4116.

[62] J. Levin, J. Chen, L. Laakso, M. Du, X. Du, A. Venkatesan, V. Sandanayaka, A. Zask, J. Xu, W. Xu, Acetylenic TACE inhibitors. Part 2: SAR of six-membered cyclic sulfonamide hydroxamates, *Bioorganic & Medicinal Chemistry Letters*, 15 (2005) 4345–4349.

[63] S. Pikul, K.L. McDow Dunham, N.G. Almstead, B. De, M.G. Natchus, M.V. Anastasio, S.J. McPhail, C.E. Snider, Y.O. Taiwo, T. Rydel, Discovery of potent, achiral matrix metalloproteinase inhibitors, *Journal of Medicinal Chemistry*, 41 (1998) 3568–3571.

[64] E. Nuti, F. Casalini, S.I. Avramova, S. Santamaria, G. Cercignani, L. Marinelli, V. La Pietra, E. Novellino, E. Orlandini, S. Nencetti, NO-isopropyl sulfonamido-based hydroxamates: design, synthesis and biological evaluation of selective matrix metalloproteinase-13 inhibitors as potential therapeutic agents for osteoarthritis, *Journal of Medicinal Chemistry*, 52 (2009) 4757–4773.

[65] N.A. Meanwell, Synopsis of some recent tactical application of bioisosteres in drug design, *Journal of Medicinal Chemistry*, 54 (2011) 2529–2591.

[66] P. Jain, C. Saravanan, S.K. Singh, Sulphonamides: Deserving class as MMP inhibitors?, *European Journal of Medicinal Chemistry*, 60 (2013) 89–100.

[67] S.L. Dixon, A.M. Smondyrev, E.H. Knoll, S.N. Rao, D.E. Shaw, R.A. Friesner, PHASE: a new engine for pharmacophore perception, 3D QSAR model development, and 3D database screening: 1. Methodology and preliminary results, *Journal of Computer-Aided Molecular Design*, 20 (2006) 647–671.

[68] R.A. Lewis, A general method for exploiting QSAR models in lead optimization, *Journal of Medicinal Chemistry*, 48 (2005) 1638v1648.

[69] V. Consonni, D. Ballabio, R. Todeschini, Comments on the definition of the Q 2 parameter for QSAR validation, *Journal of Chemical Information and Modeling*, 49 (2009) 1669–1678.

[70] P. Pratim Roy, S. Paul, I. Mitra, K. Roy, On two novel parameters for validation of predictive QSAR models, *Molecules*, 14 (2009) 1660–1701.

[71] M. Shidore, J. Machhi, K. Shingala, P. Murumkar, M.K. Sharma, N. Agrawal, A. Tripathi, Z. Parikh, P. Pillai, M.R. Yadav, Benzylpiperidine-linked diarylthiazoles as potential anti-Alzheimer's agents: synthesis and biological evaluation, *Journal of Medicinal Chemistry*, 59 (2016) 5823–5846.

[72] G.L. Ellman, K.D. Courtney, V. Andres Jr, R.M. Featherstone, A new and rapid colorimetric determination of acetylcholinesterase activity, *Biochemical Pharmacology*, 7 (1961) 88–95.

[73] H. Motulsky, Prism 5 statistics guide, 2007, GraphPad Software, 31 (2007) 39–42.

[74] R.A. Copeland, Enzymes: a practical introduction to structure, mechanism, and data analysis, *John Wiley & Sons*, 2004.

[75] F. Ferreri, C. Agbokou, S. Gauthier, Cognitive dysfunctions in schizophrenia: potential benefits of cholinesterase inhibitor adjunctive therapy, *Journal of Psychiatry and Neuroscience*, 31 (2006) 369–376.

[76] S.R. Ribeiz, D.P. Bassitt, J.A. Arrais, R. Avila, D.C. Steffens, C.M. Bottino, Cholinesterase inhibitors as adjunctive therapy in patients with schizophrenia and schizoaffective disorder, *CNS Drugs*, 24 (2010) 303-317.

[77] M.S. García-Ayllón, D.H. Small, J. Avila, J. Sáez-Valero, Revisiting the role of acetylcholinesterase in Alzheimer's disease: cross-talk with P-tau and β-amyloid, *Frontiers in Molecular Neuroscience*, 4 (2011) 22.

[78] H. Wang, R. Aslanian, V.S. Madison, Induced-fit docking of mometasone furoate and further evidence for glucocorticoid receptor 17α pocket flexibility, *Journal of Molecular Graphics and Modelling*, 27 (2008) 512–521.

[79] R.A. Friesner, J.L. Banks, R.B. Murphy, T.A. Halgren, J.J. Klicic, D.T. Mainz, M.P. Repasky, E.H. Knoll, M. Shelley, J.K. Perry, Glide: a new approach for rapid, accurate docking and scoring. 1. Method and assessment of docking accuracy, *Journal of Medicinal Chemistry*, 47 (2004) 1739–1749.

[80] N. Huang, C. Kalyanaraman, J.J. Irwin, M.P. Jacobson, Physics-based scoring of protein-ligand complexes: enrichment of known inhibitors in large-scale virtual screening, *Journal of Chemical Information and Modeling*, 46 (2006) 243–253.

[81] J. Du, H. Sun, L. Xi, J. Li, Y. Yang, H. Liu, X. Yao, Molecular modeling study of checkpoint kinase 1 inhibitors by multiple docking strategies and prime/MM-GBSA calculation, *Journal of Computational Chemistry*, 32 (2011) 2800–2809.

[82] Z. Yu, M.P. Jacobson, R.A. Friesner, What role do surfaces play in GB models? A new-generation of surface-generalized born model based on a novel gaussian surface for biomolecules, *Journal of Computational Chemistry*, 27 (2006) 72–89.

[83] P.D. Lyne, M.L. Lamb, J.C. Saeh, Accurate prediction of the relative potencies of members of a series of kinase inhibitors using molecular docking and MM-GBSA scoring, *Journal of Medicinal Chemistry*, 49 (2006) 4805–4808.

[84] G.M. Morris, D.S. Goodsell, R.S. Halliday, R. Huey, W.E. Hart, R.K. Belew, A.J. Olson, Automated docking using a Lamarckian genetic algorithm and an empirical binding free energy function, *Journal of Computational Chemistry*, 19 (1998) 1639–1662.

[85] E.M. Duffy, W.L. Jorgensen, Prediction of properties from simulations: free energies of solvation in hexadecane, octanol, and water, *Journal of the American Chemical Society*, 122 (2000) 2878–2888.

[86] C.A. Lipinski, F. Lombardo, B.W. Dominy, P.J. Feeney, Experimental and computational approaches to estimate solubility and permeability in drug discovery and development settings, *Advanced Drug Delivery Reviews*, 23 (1997) 3–25.

[87] F. Ntie-Kang, An *in silico* evaluation of the ADMET profile of the StreptomeDB database, *SpringerPlus*, 2 (2013) 353.

[88] N. Díaz, D. Suárez, T.L. Sordo, Quantum chemical study on the coordination environment of the catalytic zinc ion in matrix metalloproteinases, *The Journal of Physical Chemistry B*, 110 (2006) 24222–24230.

[89] J. Matysiak, Evaluation of electronic, lipophilic and membrane affinity effects on antiproliferative activity of 5-substituted-2-(2, 4-dihydroxyphenyl)-1, 3, 4-thiadiazoles against various human cancer cells, *European Journal of Medicinal Chemistry*, 42 (2007) 940–947.

[90] P.M. Gill, B.G. Johnson, J.A. Pople, M.J. Frisch, The performance of the Becke-Lee-Yang-Parr (B-LYP) density functional theory with various basis sets, *Chemical Physics Letters*, 197 (1992) 499–505.

[91] P. Stephens, F. Devlin, C. Chabalowski, M.J. Frisch, *Ab initio* calculation of vibrational absorption and circular dichroism spectra using density functional force fields, *The Journal of Physical Chemistry*, 98 (1994) 11623–11627.

[92] C.G. Zhan, J.A. Nichols, D.A. Dixon, Ionization potential, electron affinity, electronegativity, hardness, and electron excitation energy: molecular properties from density functional theory orbital energies, *The Journal of Physical Chemistry A*, 107 (2003) 4184–4195.

[93] Y. Zheng, M. Zheng, X. Ling, Y. Liu, Y. Xue, L. An, N. Gu, M. Jin, Design, synthesis, quantum chemical studies and biological activity evaluation of pyrazole-benzimidazole derivatives as potent Aurora A/B kinase inhibitors, *Bioorganic & Medicinal Chemistry Letters*, 23 (2013) 3523–3530.

[94] Y. Wang, X.L. Guan, P.F. Wu, C.M. Wang, H. Cao, L. Li, X.J. Guo, F. Wang, N. Xie, F.C. Jiang, Multifunctional mercapto-tacrine derivatives for treatment of age-related neurodegenerative diseases, *Journal of Medicinal Chemistry*, 55 (2012) 3588–3592.

[95] R.A. Copeland, Evaluation of enzyme inhibitors in drug discovery: a guide for medicinal chemists and pharmacologists, *John Wiley & Sons*, 2013.

[96] J. Eichler, A. Anselment, J.L. Sussman, J. Massoulié, I. Silman, Differential effects of" peripheral" site ligands on Torpedo and chicken acetylcholinesterase, *Molecular Pharmacology*, 45 (1994) 335–340.

[97] L. Di, E.H. Kerns, K. Fan, O.J. McConnell, G.T. Carter, High throughput artificial membrane permeability assay for blood-brain barrier, *European Journal of Medicinal Chemistry*, 38 (2003) 223–232.

[98] P.R. Twentyman, M. Luscombe, A study of some variables in a tetrazolium dye (MTT) based assay for cell growth and chemosensitivity, *British Journal of Cancer*, 56 (1987) 279–285.

[99] Y. Chen, J. Sun, L. Fang, M. Liu, S. Peng, H. Liao, J. Lehmann, Y. Zhang, Tacrine-ferulic acid-nitric oxide (NO) donor trihybrids as potent, multifunctional acetyl-and butyrylcholinesterase inhibitors, *Journal of Medicinal Chemistry*, 55 (2012) 4309–4321.

[100] B. Sameem, M. Saeedi, M. Mahdavi, H. Nadri, F.H. Moghadam, N. Edraki, M.I. Khan, M. Amini, Synthesis, docking study and neuroprotective effects of some novel pyrano [3, 2-c] chromene derivatives bearing morpholine/phenylpiperazine moiety, *Bioorganic & Medicinal Chemistry*, 25 (2017) 3980–3988.

[101] S. Saubern, R. Guha, J.B. Baell, KNIME workflow to assess PAINS filters in SMARTS format. Comparison of RDKit and Indigo cheminformatics libraries, *Molecular Informatics*, 30 (2011) 847–850.

[102] B.J. Alder, T.E. Wainwright, Studies in molecular dynamics. I. General method, *The Journal of Chemical Physics*, 31 (1959) 459–466.

[103] W.L. Jorgensen, D.S. Maxwell, J. Tirado-Rives, Development and testing of the OPLS all-atom force field on conformational energetics and properties of organic liquids, *Journal of the American Chemical Society*, 118 (1996) 11225–11236.

[104] K.O. Sulaiman, T.U. Kolapo, A.T. Onawole, M.A. Islam, R.O. Adegoke, S.O. Badmus, Molecular dynamics and combined docking studies for the identification of Zaire ebolavirus inhibitors, *Journal of Biomolecular Structure & Dynamics*, (2018) 1–12.

[105] A. Anantram, H. Kundaikar, M. Degani, A. Prabhu, Molecular dynamic simulations on an inhibitor of anti-apoptotic Bcl-2 proteins for insights into its interaction mechanism for anti-cancer activity, *Journal of Biomolecular Structure & Dynamics*, (2018) 1–13.

[106] U. Essmann, L. Perera, M.L. Berkowitz, T. Darden, H. Lee, L.G. Pedersen, A smooth particle mesh Ewald method, *The Journal of Chemical Physics*, 103 (1995) 8577–8593.

[107] W.G. Hoover, Canonical dynamics: equilibrium phase-space distributions, *Physical Review A*, 31 (1985) 1695.

[108] G.J. Martyna, D.J. Tobias, M.L. Klein, Constant pressure molecular dynamics algorithms, *The Journal of Chemical Physics*, 101 (1994) 4177–4189.

[109] S. Toxvaerd, J.C. Dyre, Communication: Shifted forces in molecular dynamics, in, AIP, 134, (2011) 081102 (2011), doi. 10.1063/1.3558787.

[110] A.T. Ayoub, T.J. Craddock, M. Klobukowski, J. Tuszynski, Analysis of the strength of interfacial hydrogen bonds between tubulin dimers using quantum theory of atoms in molecules, *Biophysical Journal*, 107 (2014) 740–750.

[111] D.D. Humphreys, R.A. Friesner, B.J. Berne, A multiple-time-step molecular dynamics algorithm for macromolecules, *The Journal of Physical Chemistry*, 98 (1994) 6885–6892.